Domain evolution processes in ferroelectric ceramics

Kwanlae Kim
Lincoln College

Under the supervision of Dr. John Huber

This thesis has been submitted to the University of Oxford for the degree of Doctor of Philosophy in the Department of Engineering Science

Hilary Term 2015

Domain evolution processes in ferroelectric ceramics

Kwanlae Kim, Lincoln College, University of Oxford

For the degree of D.Phil. in Engineering Science, Hilary Term 2015

Abstract

The aim of this doctoral research is to understand domain evolution processes in ferroelectrics using piezoresponse force microscopy (PFM) and Monte Carlo simulation. The results provide improved knowledge of domain evolution processes, and systematic experimental methods for research on domain evolution.

There has been extensive previous research on domain evolution in ferroelectrics, but the research was mainly constrained to simple domain patterns. However, ferroelectric domains tend to form complex patterns that generate low-energy domain configurations. In this research, several methods such as statistical analysis of PFM data, *ex situ*/*in situ* PFM observation under electrical/mechanical loading and combining PFM with electron backscatter diffraction are employed to study domain evolution processes in complex domain patterns. The results show that domain switching almost always takes place by the evolution of pre-existing domain patterns, rather than direct flipping of polarization. Also the net effect of domain evolution processes follows a primary principle that positive work is done by external loads. But this principle is not always followed for microscopic switching processes. Multiple types of domain switching occur simultaneously, and occasionally an overwriting process involves unfavourable as well as favourable domain switching. Domain switching is significantly constrained by the pre-existing domain patterns. Meanwhile, angle-resolved PFM is developed for the systematic interpretation of PFM signal. Using lateral PFM images taken from multiple sample orientations, angle-resolved PFM maps are generated based on the angle of phase reversal in the PFM signal. The resulting maps reliably show complex domain patterns which may not appear in vertical and lateral PFM images.

A model of domain evolution is developed using Monte Carlo simulation. Polarization switching by electric field and mechanical stress in the model is shown to take place *via* the motion of domain walls between pre-existing domains. Typical domain broadening processes are reproduced through this simulation.

Acknowledgements

I would like to express my gratitude to my supervisor John Huber for his help and encouragement. During my doctoral research, he always gave me unstinting support and advice. I also have learned his great attitude as a researcher as well as learning engineering. Especially, I thank him for his time spent for correcting my English in the published papers and this thesis. I also appreciate his financial support for my experimental work.

I appreciate Prof. Jin-Chong Tan and Prof. Daping Chu for their time spent for reading my thesis and viva. I would like to thank Kalin Dragnevski for training me to use several instruments and helping my experimental work. I also thank my several colleagues. First of all, I am grateful to Dan Sui for useful advice regarding experimental work. I thank Nien-Ti Tsou for helping me to understand the theoretical background of compatible domain structure. Although there was no time to work with Prashant Potnis, I also thank him for setting up the instruments in the lab, which were widely used during my doctoral research. I also thank Ananya Renuka Balakrishna for giving me some useful ideas about Monte Carlo simulation. I thank all the members in the Solid Mechanics and Materials Engineering group, and especially thank Jianan Hu and Bo Lan for helping my study.

I am very grateful to many people in Lincoln college, including the graduate officer Carmella Elan-Gaston, and the staff in the hall for providing delicious and healthy food. I would like to give special thanks to the GPs in King Edward Street Medical Practice and the doctors and nurses in John Radcliffe Hospital for their kind and special care including clarifying medical terminology for a foreign student.

I would like to express my gratitude to my mentors in Seoul National University of Science and Technology including Prof. Wonjong Joo, Prof. Dongyoung Jang, Prof. Eunkyung Kim, and Munhee Cho for motivating and encouraging my doctoral research. I will cherish the delightful memories with Korean friends including Hyunchae, Sungkyun, Minhyun, Sungho, Teasung in Oxford.

Finally, without my father and mother's unconditional support, my doctoral research would have been impossible. I deeply appreciate everything provided to me from my parents. "아버지 어머니, 항상 감사하고 사랑합니다." I also thank my sister, brother-in-law, and my nephew and niece for showing me their happy daily lives.

Contents

Table of abbreviations

2.5D	two-and-a-half-dimensional
2D	two-dimensional
3D	three-dimensional
AFM	atomic force microscopy
AR-PFM	angle-resolved piezoresponse force microscopy
BFCO	$BiFe_{0.95}Co_{0.05}O_3$
BFO	$BiFeO_3$
C-AFM	conductive atomic force microscopy
EBSD	electron backscatter diffraction
EFM	electrostatic force microscopy
ESEM	environmental scanning electron microscope
ESM	electrochemical strain microscopy
GB	grain boundary
KNN	$K_{0.5}Na_{0.5}NbO_3$
LPFM	lateral piezoresponse force microscopy
MCS	Monte Carlo step
MPB	morphotropic phase boundary
NBT	$Na_{0.5}Bi_{0.5}TiO_3$
PFM	piezoresponse force microscopy
PMN-PT	$Pb(Mg_{1/3}Nb_{2/3})O_3 - PbTiO_3$
PZT	$Pb[Zr_xTi_{1-x}]O_3$ ($0 \leq x \leq 1$) (lead zirconate titanate)
SEM	scanning electron microscopy
SPM	scanning probe microscopy
T_C	Curie temperature
TDGL	time-dependent Ginzburg-Landau
TEM	transmission electron microscopy
VPFM	vertical piezoresponse force microscopy
XRD	X-ray diffraction

Chapter 1. Introduction

Diverse devices such as biosensors [1], energy harvesters [2,3] and ultrasound transducers [4] have been developed exploiting the electromechanical coupling effect in ferroelectrics. From studies of the macroscopic behaviour of ferroelectric ceramics, non-linearity, hysteresis, and time-dependence are attributed to polarization switching and domain wall motion [5–8]. The material behaviour of ferroelectrics and hence device performance are governed by domain structures and domain wall motion [9,10]. Therefore, understanding the domain evolution processes caused by electric field and mechanical stress is central both for the development of material models and to improve device performance.

The present work focuses on the evolution process of low-energy domain configurations in near-morphotropic polycrystalline bulk lead zirconate titanate (PZT)[1]. The key question tackled in the research is whether existing, energy based, models of domain switching correctly describe the microscopic processes of ferroelectric switching. Through experimental work and simulations, the underlying evolution mechanisms are studied. In this chapter, some background about ferroelectrics and domain structure is introduced. Then the primary principle of domain switching is discussed, and the main question for the present research is raised. Piezoresponse force microscopy (PFM) and Monte Carlo simulation are introduced as the main techniques used for the research. Finally, the layout of the thesis is introduced.

[1] A table of abbreviations and their meanings are provided after Contents and before Chapter 1.

1.1 Introduction to ferroelectric crystals

Piezoelectric materials generate electrical effects under mechanical stress due to having a non-centrosymmetric crystal structure [11]. Ferroelectrics are piezoelectric materials in which spontaneous polarization occurs and the polarization is reversible by electric field. Ferroelectricity was first discovered in Rochelle salt by Joseph Valasek [12]. More recently, PZT has been one of the most used ferroelectric ceramics due to its superior material properties including high piezoelectric constant [13]. Ferroelectrics can be divided into four main groups by the structure of their unit cell, and PZT belongs to ABO_3 perovskite group. As shown in figure 1.1, the unit cell of PZT consists of six O^{2-} ions at the centre of faces, eight Pb^{2+} ions at each corner (A site), and Zr^{4+}/Ti^{4+} ion (B site). The Zr^{4+}/Ti^{4+} ions are located at the centre of the oxygen octahedron when the temperature is above Curie temperature T_C, where phase transition between paraelectric and ferroelectric occurs. As the material is cooled below T_C, the displacement of Zr^{4+}/Ti^{4+} ions occur along certain crystallographic directions. The off-centre displacement of a charged ion gives rise to a net dipole moment per unit volume, or spontaneous polarization. When spontaneous polarization happens, spontaneous strain is simultaneously generated, distorting the unit cell. Figure 1.1 shows the transformation from cubic to tetragonal crystal structure in PZT *via* spontaneous polarization and strain.

The phase in PZT is dependent on the compositional ratio between $PbZrO_3$ and $PbTiO_3$. As the phase diagram in figure 1.2 shows [14], PZT is in the tetragonal or rhombohedral phase at room temperature. In the tetragonal phase, Zr^{4+}/Ti^{4+} ions are displaced in the <001> directions, while in the rhombohedral phase, the Zr^{4+}/Ti^{4+} ions are displaced along the <111> directions. These two phases are separated by a

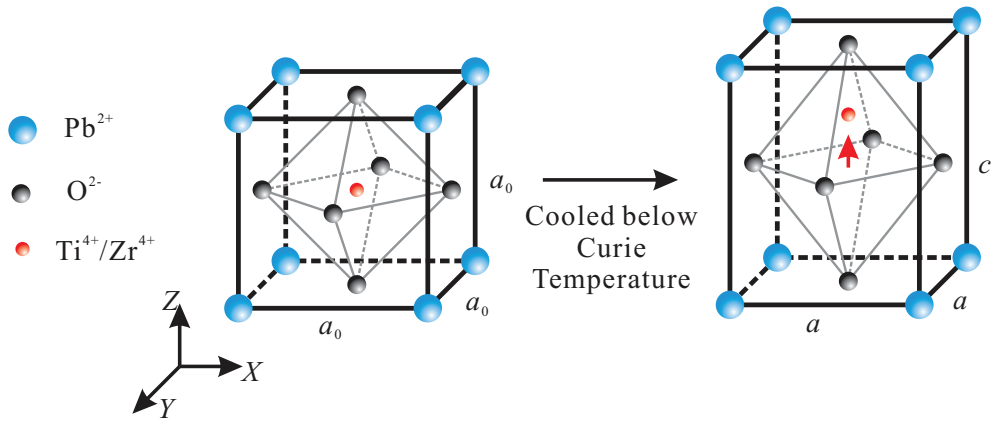

Figure 1.1: Transformation from paraelectric phase above the Curie temperature (T_C) to ferroelectric below T_C in PZT.

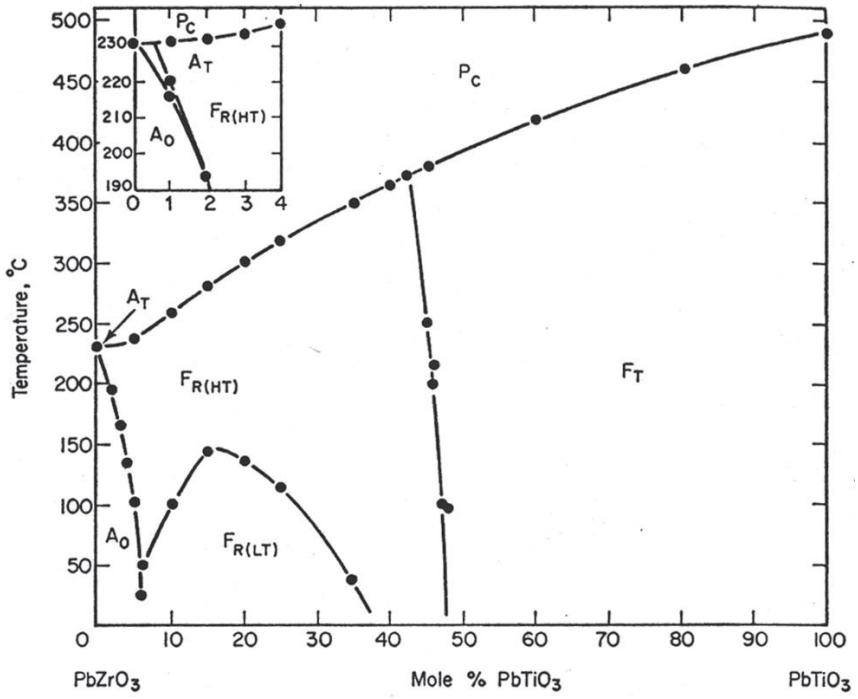

Figure 1.2: Phase diagram of PZT [14]. A_O and A_T indicate orthorhombic and tetragonal antiferroelectric phases, respectively. $F_{R(HT)}$ and $F_{R(LT)}$ represent rhombohedral ferroelectric phases at high and low temperature, respectively, separated by electrical properties and thermal expansion. F_T is the tetragonal ferroelectric phase and P_C indicates the cubic paraelectric phase.

morphotropic phase boundary (MPB). In near-MPB PZT, the tetragonal and rhombohedral phases can co-exist at room temperature [15,16], allowing the material to be easily polarizable in any <100> or <111> direction. The resulting freedom to adopt

many spontaneous polarization and strain states gives ceramics with high overall polarization, and high strain capability. The majority of piezoelectrics in commercial applications are near-MPB PZT. However, from the point of view of scientific investigation, the mixture of phases presents an additional degree of complexity in identifying ferroelectric microstructure in this material. In isothermal conditions the equilibrium phase can change due to slight variations in composition, or local residual stresses and electric fields [17].

A ferroelectric domain can be defined as a region with a uniform electrical polarization. Whenever two distinct domains neighbour, a thin boundary called a domain wall forms. Domain walls can be divided into two types: 180° and non-180° [18]. These two types of ferroelectric domains arise for different reasons. Changes in spontaneous polarization produce surface charge density that results in depolarization field. The energy associated with depolarization field is minimized by having 180° domains as shown in figure 1.3(b) and figure 1.4. By contrast, non-180° domain structures are generated due to stress that is often generated during phase transformation by cooling [18]. These structures relieve stress by allowing the crystal to adopt different shapes.

1.2 Identifying domains and domain walls

In this work, one of the major challenges tackled is the identification of domain patterns from images of microstructure. A brief introduction to the theory of compatible domains is given here since a knowledge of the appearance and organization of domain patterns helps in interpretation of the microstructure images in this thesis. When multiple ferroelectric domains are present, the total energy in the microstructure can be minimized by forming particular domain configurations. To achieve energy minimization, a domain

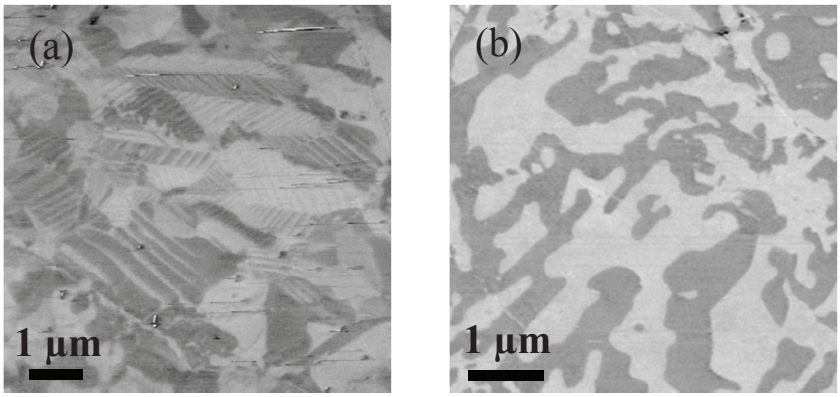

Figure 1.3: (a) Non-180° and (b) 180° domain pattern, observed in PZT by PFM.

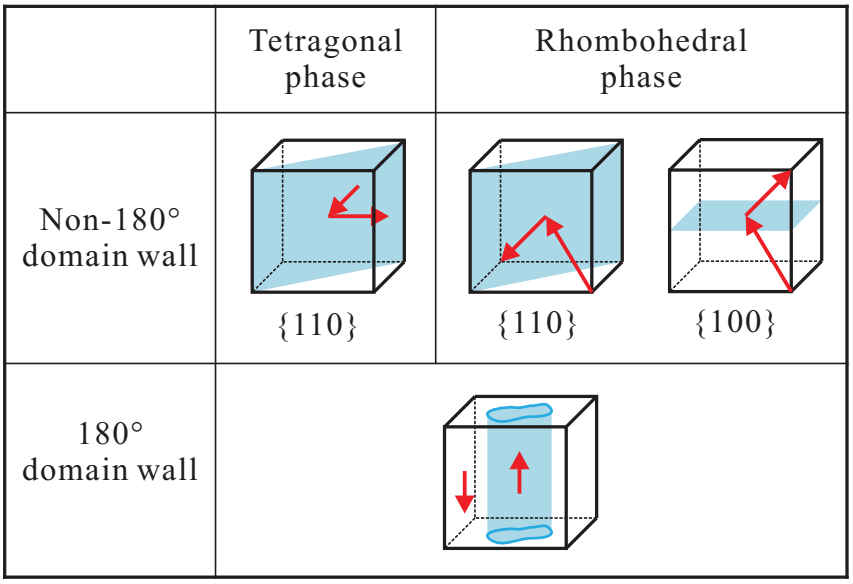

Figure 1.4: Compatible non-180° and 180° domain wall in tetragonal and rhombohedral.

wall must satisfy electrical and mechanical compatibility conditions [19,20]. For a pair of domains i and j with the spontaneous strain states $\boldsymbol{\varepsilon}_i, \boldsymbol{\varepsilon}_j$, and spontaneous polarization vectors $\mathbf{p}_i, \mathbf{p}_j$, the interface normal vector, $\mathbf{n}$, which produces a minimum energy, compatible arrangement of domains, satisfies [21]

$$\boldsymbol{\varepsilon}_i - \boldsymbol{\varepsilon}_j = \frac{1}{2}\left(\mathbf{a}\otimes\mathbf{n} + \mathbf{n}\otimes\mathbf{a}\right), \tag{1.1}$$

and

$$\left(\mathbf{p}_i - \mathbf{p}_j\right)\cdot\mathbf{n} = 0, \tag{1.2}$$

where **a** can be any vector chosen to satisfy equation (1.1). A unique domain wall orientation, **n**, can be obtained by solving equations (1.1) and (1.2) except for the case $\boldsymbol{\varepsilon}_i = \boldsymbol{\varepsilon}_j$. In this case, equation (1.1) can be solved by setting $\mathbf{a} = 0$, and equation (1.2) gives a continuous set of solutions for **n**. Such identical spontaneous strain states across a domain wall are found wherever the polarization directions are antiparallel, as in 180° domain structure. Thus, there is no habit plane for 180° domain walls and they typically appear as curvy lines in microstructure images [22,23]. This is shown in figure 1.3(b). By contrast, non-180° domain walls are straight, as can be seen in figure 1.3(a). Solving equations (1.1) and (1.2) in the rhombohedral crystal system with <111> polarization vectors shows that non-180° domain walls can form in the {110} or {100} planes, see figure 1.4. In the tetragonal crystal system, with <100> polarization vectors, non-180° domain walls can only form in {110} planes. Thus, finding the crystallographic plane in which a domain wall lies can assist in identifying the domains on either side. But note also that non-180° domain walls can form in the {110} planes in either tetragonal or rhombohedral phase, and so their presence would not distinguish between these two phases.

Complex domain patterns often consist of multiple crystal variants forming laminations. In such cases a binary tree diagram [19,24] is a useful tool to describe domain configurations, see figure 1.5. Here the four arrows in the lowest level, labelled "rank-0", represent four in-plane polarization vectors of distinct crystal variants in the tetragonal phase. Taking the pure crystal variants as rank-0, a simple lamellation composed of two distinct variants is a rank-1 microstructure. The herringbone domain pattern shown in figure 1.5 consists of two differently oriented lamellations joined together to form a rank-2 pattern. Previous work [21] has shown that a very limited number of such patterns can form compatibly in the tetragonal and rhombohedral crystal

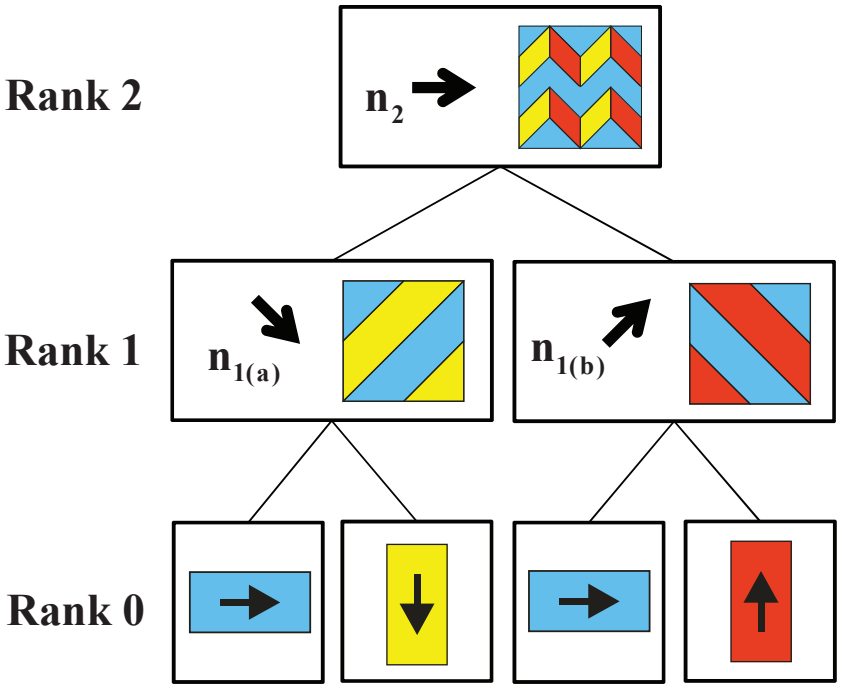

Figure 1.5: A binary tree for rank-2 lamellar domain structure where $\mathbf{n}_i$ is the interface normal vector of rank i domain wall.

systems, so they are relatively easy to identify. For the interpretation and explanation of the observed domain patterns, the compatibility theory of multi-rank lamellar structures is employed in this thesis; see [19,21] for further details.

1.3 Poling and piezoelectricity

In their initial state after sintering, ferroelectric ceramics consist of multiple domains with randomly oriented polarizations, and hence polarizations cancel on average making the net polarization zero. This random state has the consequence that ferroelectrics may not exhibit piezoelectric response at the bulk scale even though each domain has piezoelectricity. However, ferroelectric materials can be transformed into active piezoelectric materials by aligning the polarized domains through an externally applied electric field. This process is called 'poling' [18]. Since polarization directions are

constrained to certain crystallographic orientations, poling typically aligns polarization directions along the electric field direction as closely as possible, but not exactly.

The poled ferroelectrics then behave as piezoelectric materials. The direct and converse piezoelectric effects in ferroelectrics can be described as follows, respectively [11,25]:

$$D_i = d_{ikl}\sigma_{kl} + \kappa_{ik}^{\sigma} E_k, \tag{1.3}$$

$$\varepsilon_{ij} = s_{ijkl}^{E}\sigma_{kl} + d_{kij} E_k, \tag{1.4}$$

where D_i is the electric displacement, d_{ikl} is the piezoelectric constant, σ_{kl} is the stress, κ_{ik}^{σ} is the dielectric constant with the stress held constant, E_k is the electric field, ε_{ij} is the strain, s_{ijkl}^{E} is the elastic compliance with the electric field held constant. All of the quantities in equations (1.3) and (1.4) are tensors of various ranks. The indicial notation $(i, j, k, l = 1\ldots3)$ is used and summation over repeated indices is implied. Hence electric field E_k and electric displacement D_i, which are vectors, have a single index. The piezoelectric tensor d_{ikl} is a rank-3 tensor, and so forth. The direct piezoelectric effect in equation (1.3) indicates that externally applied stress generates a net electric displacement. Reversely, the converse piezoelectric effect in equation (1.4) represents a change in the net strain caused by externally applied electric field.

1.4 Ferroelectric switching at the macroscopic scale

For a near MPB composition of soft polycrystalline PZT, designated PZT-855 and distributed by APC International, the change in the net electric displacement (D_3) and a change in the net strain (ε_{33}) during cyclic electrical loading (E_3) are shown in

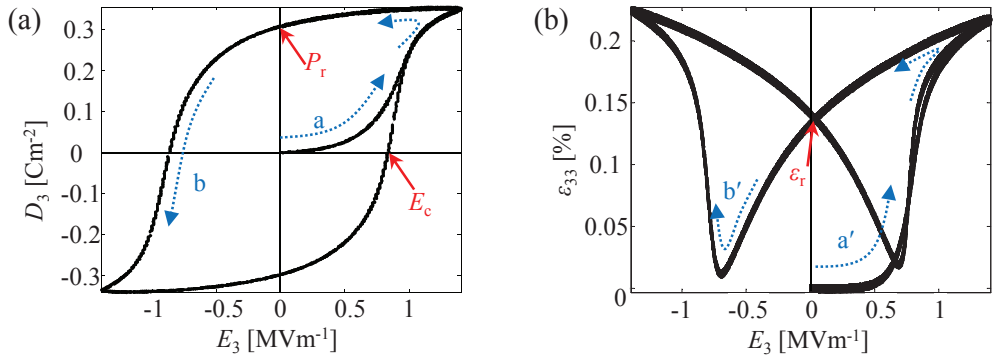

Figure 1.6: (a) Measured electric displacement (D_3) versus electric field (E_3) and (b) Measured strain (ε_{33}) versus electric field (E_3) of PZT-855, with no mechanical loading.

figures 1.6(a) and (b), respectively. For these measurements, blocks of unpoled PZT were cut out using a diamond saw. Silver electrodes were painted on the opposite faces of the blocks. A strain gauge was applied to the one of the polished surfaces measuring along the electric field direction using Cyanoacrylate adhesive. The sample was held in transformer oil and the two electrodes were connected to a high voltage amplifier and an electrometer. Meanwhile, the strain gauge was connected to a quarter Wheatstone bridge and data logger. In figure 1.6(a), D_3 increases in a non-linear fashion with an increase of E_3 in the section a, that is called "virgin curve". The graph shows the hysteresis response of D_3 by alternating E_3 . In figure 1.6(a), there are two different states of electric displacement at zero electric field; when $E_3 = 0$, $D_3 = \pm P_r$, where P_r is called the remnant polarization. These two distinct states in ferroelectrics are exploited in non-volatile random access memory [26]. To make $D_3 = 0$, a certain amount of electric field is required during the polarization reversal marked b in figure 1.6; this is the coercive electric field (E_c). The value of E_c is sensitively affected by domain structures and wall motion [27] as well as loading frequency and the presence of stress.

Meanwhile, ε_{33} increases non-linearly during the virgin curve (a′), and remains at the remnant strain ε_r when E_3 returns to zero. One interesting point in this graph is the

section b′, where ε_{33} dips to almost zero. Such a narrow v-shaped curve is attributed to non-180° polarization switching [8], indicating that electric field can induce both 90° and non-180° polarization switching.

1.5 Domain switching at the microscopic scale

A domain is defined as a region where a uniform polarization direction is present. Domain switching refers to a switching from one polarization direction to the others. Domain switching can be induced by externally applied electric field or mechanical stress due to electromechanical coupling effect in ferroelectrics. In this thesis, the name "primary principle" of domain switching is used to describe the concept that switching occurs in such a way that external loads do positive work on the material. For example, in a tetragonal crystal structure, uniaxial compressive stress tends to reorient the spontaneous strain such that the shortest axis is parallel to the loading axis. Similarly externally applied electric field aligns the polarization direction as nearly as possible parallel to the field direction. In figure 1.7, each hexagonal unit represents a single grain consisting of multiple domains at an unpoled state. By poling, these randomly oriented polarizations are aligned towards the electric field *E via* 180° and non-180° switching as figures 1.7(b) and (c) show, respectively. The process causes electrical work to be done by the external electric field. In this poled state, compressive stress can depolarize the material, by switching polarization directions such that the short axis of the unit cell is parallel to the loading direction, see figure 1.7(d). In this case, the external stress does mechanical work. Both of these examples can be summarized using the primary principle: "switching occurs such that external loads do positive work." This principle appears to be widely adopted in the interpretation of macroscopic ferroelectric/ferroelastic switching,

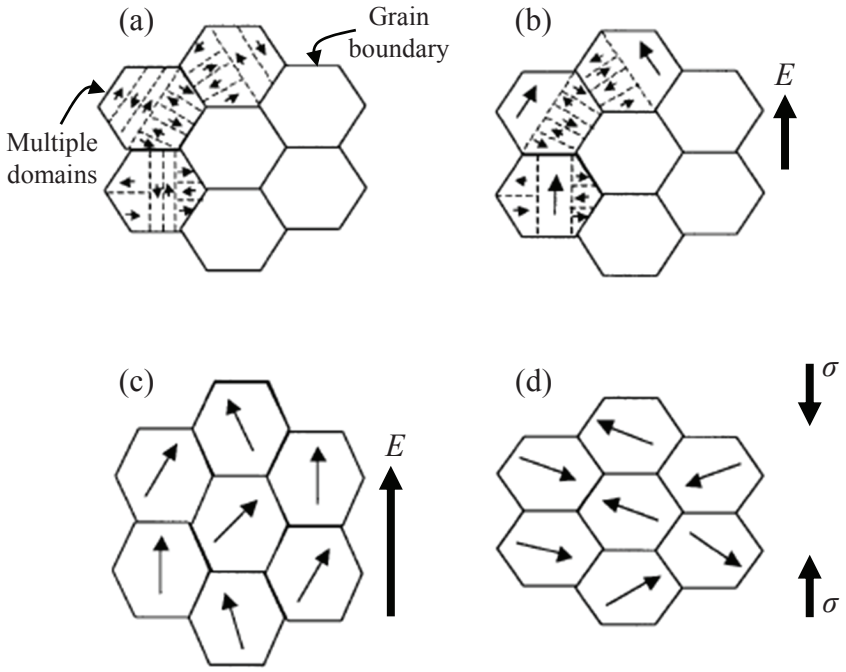

Figure 1.7: Domain switching by electrical or mechanical loading. (a) Multiple domains in an unpoled polycrystalline ferroelectric. (b) 180° domain switching by electric field. (c) Non-180° domain switching by increased electric field. (d) Depolarizing the poled ferroelectric by compressive stress (modified from Moulson *et al*. [18]).

often without explicitly stating the principle [6,8,18,28,29]. One purpose of the present study is to test to what extent this primary principle holds at the microscopic level.

To understand the relationship between domain switching and the macroscopic behaviour of ferroelectrics, a polarization switching criterion under electrical and mechanical loading was proposed by Hwang *et al.* [6]. In Hwang's work, changes in the net polarization and strain were studied during electrical and mechanical loading. Hwang's switching criterion is [6]

$$E_i \Delta D_i + \sigma_{jk} \Delta \varepsilon_{jk} \geq G_c, \tag{1.5}$$

where E_i is the applied electric field, ΔD_i is the change in spontaneous polarization, σ_{jk} is the applied stress, $\Delta \varepsilon_{jk}$ is the change in spontaneous strain, and G_c is a critical threshold

value for switching to occur. When only electrical loading is considered, equation (1.5) becomes

$$E_i \Delta D_i \geq G_c . \tag{1.6}$$

Hwang's switching criterion indicates that as the magnitude of electric field is increased, the most favourable switching event (that with the greatest value of $E_i \Delta D_i$) will happen first, followed by less favourable switching events at higher electric field. Models based on Hwang's criterion and related energetic statements make reasonable predictions of ferroelectric switching at the macroscopic scale [6]. However, there is currently little evidence available to test whether switching really follows this criterion at the microscopic scale. The present work sets out to explore the validity of such energetic criteria at the microscopic scale.

Domain switching normally takes place by a domain wall sweeping across domains [30–32]. The previous works [33–35] show that in two neighbouring domains, one domain can grow over another domain through broadening and lengthening of lamellae. Such a simple domain wall motion in a rank-1 lamination domain pattern can be explained by equation (1.5). However, it is still elusive to understand how more complex domain patterns evolve by electrical or mechanical loading. This is because complex domain patterns such as checkerboard and herringbone patterns can be found in polycrystalline materials. Unlike the simpler lamellar patterns these complex patterns often cannot undergo switching through the motion of a single domain wall. They require careful experimental study to reveal the evolution mechanism of domain patterns at sub-micron scale. Thus, in this thesis multiple characterization techniques including atomic force microscopy (AFM), PFM, electron backscatter diffraction (EBSD), and optical

microscopy were employed for qualitative and quantitative analysis of domain switching in polycrystalline PZT.

1.6 Characterization techniques

Visualizing ferroelectric domain patterns is essential to understand the microstructure in ferroelectrics. Various imaging techniques for ferroelectric domains have been discussed in detail by Potnis *et al.* [36] and Soergel [37]. Visualizing methods can be divided into three groups by the material properties of ferroelectrics that are used for the imaging process [37].

The first property is spontaneous polarization. Polarized domains generate surface charge that can be exposed *via* surface decoration with powders such as sulfur or lead oxide [38], or with liquid crystals [39]. Alternatively, electrostatic force microscopy (EFM) [40] can reveal the surface polarization. Another way of utilizing spontaneous polarization is by etching the surface of ferroelectric materials. This method takes advantages of different etching rate on the positive or negative end of the dipole that causes electric polarization. For example, etch rate of hydrochloric acid at the positive end of the polarization is faster than that at the negative end in $BaTiO_3$ [41]. The domain structures exposed through etching can then be observed using optical or electron microscopy, or AFM. However, etching is a destructive method, and hence not ideal for observing domain evolution.

Secondly, locally-induced surface displacement by the converse piezoelectric effect can be used for mapping domain structures. For example, in a scanning probe microscope alternating voltage can be applied to the surface of a ferroelectric through the conducting tip, to generate local strain. This technique is PFM [42], that is one of the

most widely used imaging techniques for ferroelectric domains [43]. The converse piezoelectric effect is also exploited in scanning electron acoustic microscopy [44] and scanning near-field acoustic microscopy [45], where acoustic waves generated by local strain are used for imaging.

Finally, the refractive index is affected by local strain state, and hence non-180° domain patterns in transparent materials such as single crystal $BaTiO_3$ can be observed through optical microscopy. Accordingly, 180° domain patterns are not clearly observed through this method unless an external electric field is applied to take advantage of electro-optic effect [37,46].

Currently, the most widely used methods for imaging ferroelectric domains are scanning probe microscopy (SPM), optical microscopy, and electron microscopy. Among several scanning modes in SPM, PFM has been the most successful due to high resolution. PFM typically provides resolution < 100 nm [47–50], and is capable of resolving both 180° and non-180° domain structures. Additionally, it requires only surface polishing for the sample preparation. However, the imaging speed is limited by the scan speed, and hence is not advantageous in *in situ* observation of domain evolution compared to optical microscopy. High-speed PFM, capable of 1 frame per second, has been used for *in situ* observation of domain switching to overcome this drawback by scanning without feedback [51–53].

By contrast with SPM, optical microscopy is advantageous in a real-time observation of domain evolution since it does not involve scanning. In addition, domain structures can be observed without physical contact with the sample surface, and hence the optical method is suitable for *in situ* observation of domain wall motion by mechanical stress [54] or electric field [55]. However, the critical weakness of optical microscopy lies in lateral resolution, typically ~1 μm [37]. Also, domain patterns in

opaque materials are not observed by optical microscopy unless the material is etched or decorated.

Scanning electron microscopy (SEM) [56] is also used to study domain patterns and domain evolution. The scan speed of SEM is in general faster than that of typical SPM, and hence it is more suitable than SPM for observing domain evolution. However, the incident electron beam can cause charge build-up on the surface of ferroelectrics, and hence the initial domain structure can be altered. EBSD is a SEM-based technique that identifies crystallographic orientation of grains using the diffraction of electrons by the lattice planes [57]. This technique does not provide resolution as high as other electron microscopy, but can enable us to identify the crystallographic orientations of individual domains [58]. Transmission electron microscopy (TEM) is another technique that uses electrons to characterize materials. Since much larger accelerating voltage (typically 100–400 keV) compared to SEM (usually 1 keV) is used, high resolution images can be generated from TEM. This enables studying the properties of domain walls on the atomic scale [59], and domain wall distortion during evolution process by externally applied electric field [60]. Another advantage of TEM is that the imaging process does not require any direct physical contact between the instrument and the specimen. Thus, *in situ* observation of domain wall motion by externally applied electric field has been conducted using TEM [34,61,62]. However, in TEM specimens should be very thin (typically 10–300 nm) for electrons to pass through, and hence sample preparation tends to be complicated, while the applicability to bulk ceramics is limited.

Finally, X-ray diffraction (XRD) and related neutron diffraction technique identifies crystal structure by measuring lattice parameters. This technique has been extended to the research of phase evolution, domain switching, lattice strains and so on [63]. Domain switching by electric field in PZT has been quantitatively studied by

analyzing the intensity of diffraction peaks from X-ray [64,65]. Qualitative study can be also conducted through XRD imaging. For example, both 180° and non-180° domain patterns were observed from $BaTiO_3$ [66] and strontium barium niobate [67]. The main merit of XRD technique is that domain patterns in the interior of the crystal can be also observed. Therefore, the differences between the domain pattern in the surface and that in the interior of the crystal can be studied [67]. Neutron diffraction has similar capabilities, with the advantage that the radiation easily penetrates through thick samples. However, the spatial resolution is limited compared with XRD.

1.7 Piezoresponse force microscopy

AFM [68] that measures surface topography is the basic mode in SPM. The operational principle of AFM is shown in figure 1.8. The tip scans the material surface in a raster fashion, and this process is controlled by an *x–y* piezo scanner. The vertical movement of the scanning probe is detected through the reflection of the laser beam onto the photodetector, and the vertical position is controlled by the set-point. The difference between the actual behaviour of the scanning probe and the set-point is used as the source of topography images, and the vertical position of the scanning probe is continuously adjusted to remove this difference [69].

Various types of microscopy in SPM can be divided into contact mode, tapping mode, and lift mode. In contact mode, the tip scans in contact with the material surface while in tapping mode the scanning probe oscillates and taps the material surface. Contact mode is advantageous in fast scan, but the tip is more vulnerable to damage. Thus, tapping mode is occasionally essential when imaging soft samples even though the scan speed is slower than contact mode. In SPM, a certain set-point is maintained through the

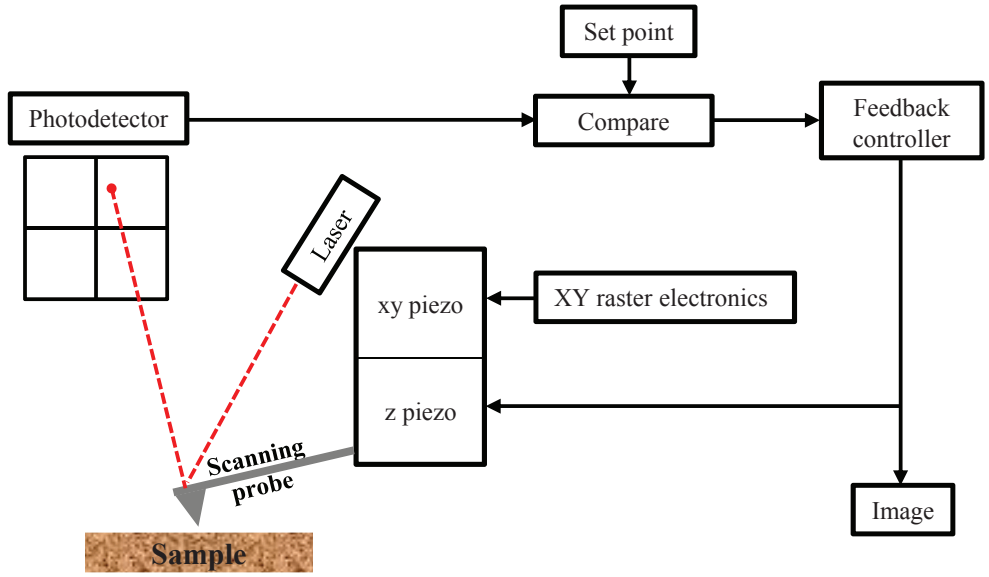

Figure 1.8: Schematic of AFM (modified from [69]).

feedback circuit to protect the tip and the material surface from damage. In contact mode, a cantilever deflection set-point is used while in tapping mode the amplitude of cantilever oscillation set-point is used. When the distance between the tip and the sample surface is required to stay constant for characterizing electrical properties of materials, lift mode is used [70]. In this mode, the topography data is collected from a first scan in contact mode, followed by the second scan in lift mode measuring the material property of interest.

Diverse SPM techniques have been developed for the electrical characterization of functional materials [70]. For example, the dopant density in semiconductors such as gallium nitride can be profiled using scanning capacitance microscopy by measuring the magnitude of capacitance in the oxide layer between the metal-coated tip and the semiconductor surface [71]. And conductive AFM (C-AFM) is used to measure the conductivity of nanostructures such as nanowires [72]. Magnetic force microscopy operates in lift mode, characterizing magnetic domains by measuring the magnetic force between a tip coated with a ferromagnetic material and the magnetic structure in the material surface [73,74]. Meanwhile, ferroelectric domain structures can be visualized through EFM [40] or PFM [42]. One of the main differences between these two

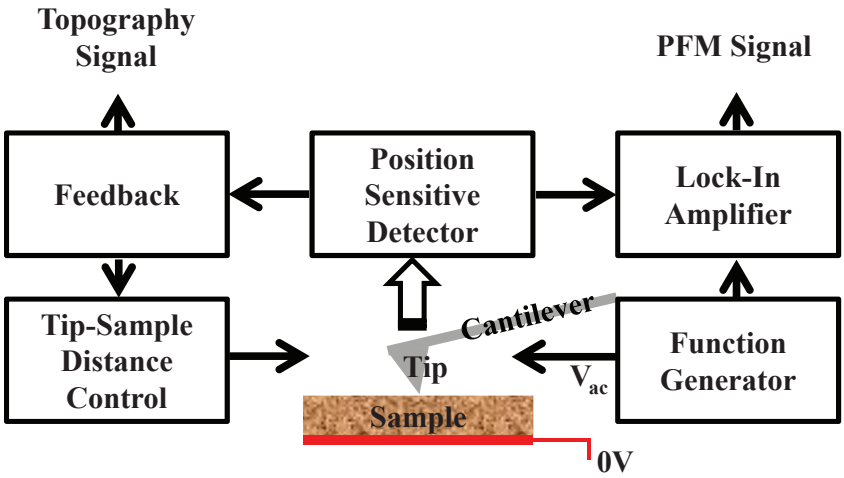

Figure 1.9: Schematic of simultaneous imaging process of AFM and PFM (modified from [42]).

techniques is that EFM operates in lift mode and PFM in contact mode. PFM is preferentially used for imaging ferroelectric domains due to the outstanding lateral resolution.

PFM works by exciting the local converse piezoelectric response of a surface using an oscillating voltage applied to the scanning probe cantilever tip. Since this induces oscillating mechanical displacements in the surface, the contacting tip also oscillates at the driving frequency; the amplitude and phase of these oscillations provide the PFM signal. The cantilever motion is monitored through the reflection of laser light from the cantilever onto a photodetector. The resulting PFM signal is distinguished from the topography signal by filtering the signal at the driving frequency, using a lock-in amplifier as shown in figure 1.9.

In PFM, the amplitude signal (A/V_{ac}) is in the units of nm/V , where A is the deflection amplitude from the tip motion and V_{ac} is the alternating voltage applied to the scanning probe. A phase signal (φ) can be obtained separately, or as a mixed signal, in the form $(A\cos\varphi)/V_{ac}$ [75,76]. The principle of the lock-in amplifier is introduced in appendix A.1. To avoid phase dependency of the output signal, two signals are generated

from the lock-in amplifier: $X = R\cos\varphi$ and $Y = R\sin\varphi$. The magnitude and phase are then $R = (X^2 + Y^2)^{1/2}$ and $\varphi = \tan^{-1}(Y/X)$, respectively [42,77].

The phase signal represents the phase difference between the input voltage V_{ac} and the resulting piezoresponse signal. In vertical PFM (VPFM), depending on whether the vertical component of the local surface displacement is into-plane or out-of-plane relative to the sample surface, the relationship between V_{ac} and the piezoresponse signal is either in-phase or out-of-phase. Therefore, the phase image ideally consists of only two values separated by 180°. However, in practice typical PFM images show a gradual variation of phase signal (This will be discussed in detail in chapter 4).

PZT has one of the largest values of piezoelectric constant among all ferroelectrics, but d_{33} in tetragonal PZT 40/60 is still only about 160 pm/V [78]. To amplify the resulting tiny surface oscillation, the resonance of the scanning probe and surface induced by the converse piezoelectric effect is exploited. This resonance is called contact resonance, and the corresponding operating frequency is the contact resonance frequency.

A surface displacement induced by local converse piezoelectric effect can be decomposed into one out-of-plane and two in-plane components. The out-of-plane and in-plane component contributes to cantilever bending and torsion, respectively. In VPFM the vertical (out-of-plane) oscillations due to cantilever bending are measured, while lateral PFM (LPFM) data is derived from the torsional oscillations of the cantilever. Consequently, LPFM data relates to in-plane surface displacements that are perpendicular to the cantilever. Since VPFM only reveals the vertical component of surface displacement, multiple domains with the same vertical component of surface displacement would not be clearly distinguished by VPFM. In this case, these domains can be exposed through the distinct lateral component of surface displacement using

LPFM. LPFM from a certain sample orientation provides only the in-plane component of surface displacement perpendicular to the cantilever. Therefore, further information about the in-plane surface displacement vector can be gained by taking a second LPFM scan after rotating the sample by 90°. These two LPFM scans and one VPFM scan can provide 'three-dimensional' surface displacement data, and this technique is called three-dimensional (3D) PFM [79,80].

To identify the in-plane vector of surface displacement using LPFM from two orthogonal sample orientations, the amplitude of the signals must be quantified. However, LPFM signals are subject to artefacts due to the tip-surface contact such as tip sliding, and the torsion will saturate at some point [75]. Therefore, even if two LPFM scans from orthogonal directions are conducted, an accurate in-plane surface displacement vector cannot necessarily be identified. To overcome this problem, angle-resolved PFM (AR-PFM) will be used and developed in this thesis to identify ferroelectric domain structures. This will be discussed in detail in chapter 4.

1.8 Simulation of domain evolution

Simulations using materials modelling techniques help understanding the physics underlying experimental results. Additionally, for situations that are difficult to achieve in experiments, results can still be predicted through simulations. In this thesis, modelling was carried out to support interpretation of the domain evolutions observed from PFM and to test whether energy based switching rules could reproduce effects similar to the PFM observations. Specifically, a Monte Carlo method was tested for modelling ferroelectric domain evolution. As a way of introducing and motivating the energetic Monte Carlo method, several modelling methods are briefly reviewed here, starting with

models at the grain/microstructure scale and progressing towards models that resolve individual domains.

In micromechanical modelling, the properties of a material are related to the properties of its constituent parts [81]. In ferroelectrics, the large scale measurable quantities such as strain and polarization can be related to those of microscopic grains. By modelling materials based on their microstructure, the influence of the microstructure on the macroscopic material behaviour can be studied. Hwang's switching model [6] is one of the most well-known micromechanical models among the early works. In this model, each grain is taken to consist of a single domain, and all are subjected to uniformly applied stress or electric field. Whenever a grain surpasses an energy based switching criterion, which was given in equation (1.5), switching takes place. However, this model had limitations in that domains and domain wall motion were not considered. This aspect was incorporated later through constitutive models [82–84] having multiple domains within each grain. However, these models used volume fractions to represent the domains and so did not describe specific domain structures.

The modelling methods that describe ferroelectric domain structures and their evolution can be divided into two classes: sharp interface and diffuse interface models, depending on how domain walls are treated [36]. In sharp interface models [19,21,85–87], a ferroelectric domain wall is regarded as a discontinuous boundary across which there are sudden changes in polarization and strain. The fine structure of the domain walls does not have to be resolved in sharp interface models, and this typically reduces the amount of computation required. Evolution processes for low-energy domain configurations by electrical loading were studied with the sharp interface model [87]. Figure 1.10 shows an example of a sharp interface model used to study domain wall motion during switching of a single crystal from the reference [87]. The main drawback of sharp interface model is

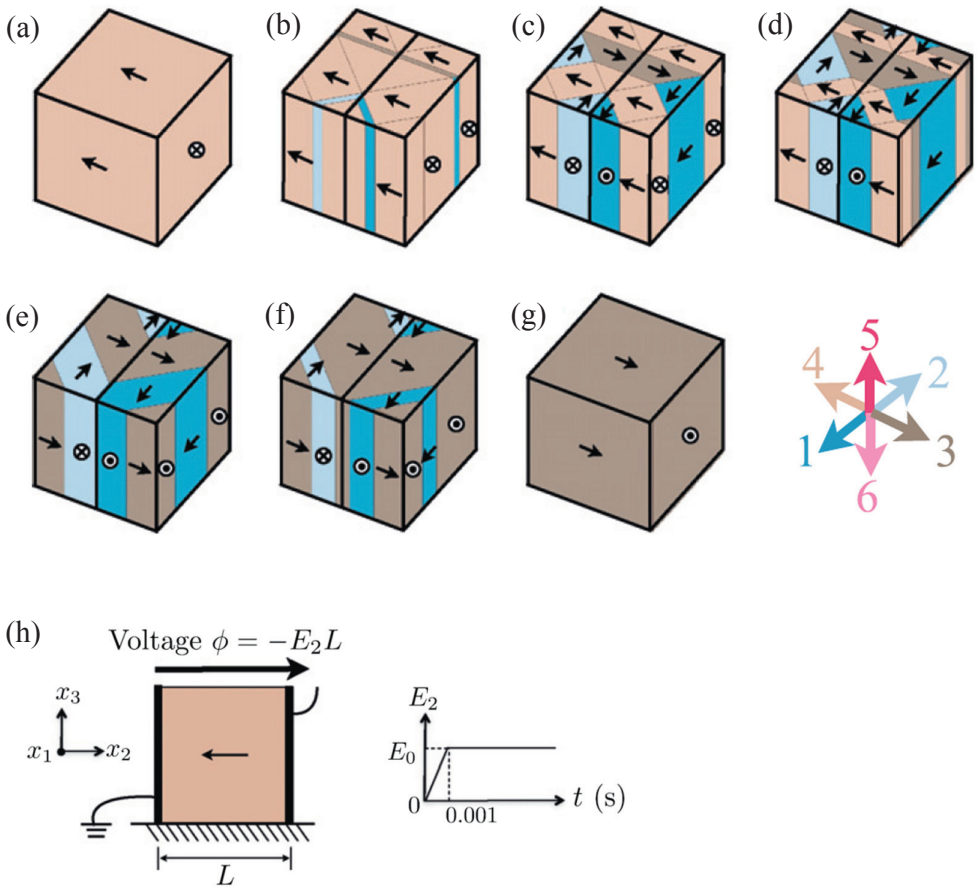

Figure 1.10: A modelling study of domain evolution under electric field using sharp interface method. (a)–(g) show the evolution of domain structures during a switching process, and (h) is the simulation set-up (modified from [87]).

the need to track interfaces, which is not difficult for laminates but more complicated for needle-like structures and curved walls.

By contrast, in diffuse interface models, domain walls are treated as having continuously varying polarization and strain [36]. In particular, the phase field method has been widely used to study material processes such as grain growth and solidification, and has been preferentially used among the diffuse interface models for studying ferroelectric domains [88–92]. In the phase field model, the total free energy in a crystal consists of various energy terms. The order parameter, typically polarization in ferroelectric domain walls, evolves to minimize the total free energy through the time-dependent Ginzburg-Landau (TDGL) equation. However, the size of a ferroelectric

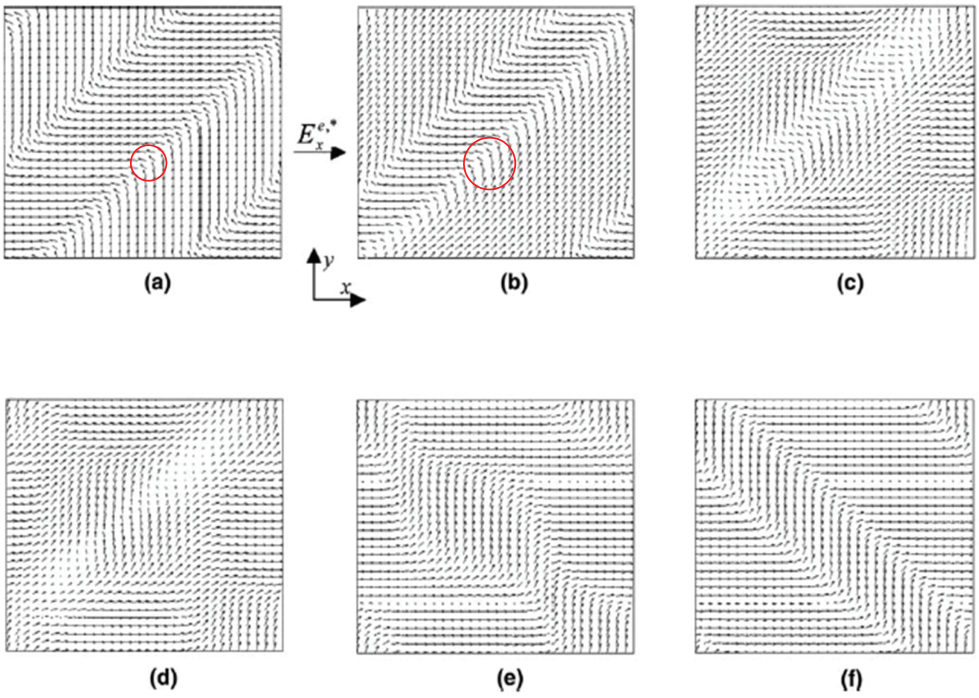

Figure 1.11: A study of domain evolution by an externally applied electric field $E_x^{e,*}$ using the phase field method. The six images show temporal evolution of domain switching: (a) initial state; (b) 70 steps; (c) 100 steps; (d) 110 steps; (e) 140 steps and (f) 200 steps. The domain walls marked by circles in (a),(b) are resolved in detail by the phase field method (modified from [28]).

domain wall is typically of order of a few lattice parameters, and in numerical studies the mesh size should be finer than the width of domain wall to resolve it in the phase field model. Thus, a major drawback of the phase field model is intense computation, limiting this approach to regions typically nm in scale. Hence the approach is not well suited for studying complex domain configuration on the μm scale. An example of studying the evolution of domain patterns under electric field using phase field methods is illustrated in figure 1.11 [28].

In Monte Carlo simulation, a physical process takes place according to the variable that is defined in a stochastic way. In physical sciences, many processes such as diffusion limited aggregation are effectively explained using Monte Carlo method, and hence this method has been widely applied to various problems [93]. In the present work, a Monte Carlo method was used as an alternative to the sharp interface and phase field

methods to study the evolution of ferroelectric domain structure. Monte Carlo method provides a few advantages for working on domain evolution in ferroelectrics. First of all, Monte Carlo method drives the transition toward minimizing the total energy, but does not always reduce energy on every step. Therefore, this method can find 'global' minimum energy by stepping over energy barriers. Secondly, in the transition process by Monte Carlo method, thermal energy plays an important role. Thus, temperature can be naturally incorporated into material models. Third, the typical size of low-energy domain configuration in PZT was > 1 μm. In some materials such as barium titanate, the size is much larger than that of PZT. Thus, it would require a large computation time if each unit cell is represented by a lattice point. But in the Monte Carlo method, it is possible to make a lattice point represent a finite volume corresponding to several or many unit cells. This allows the method to be adapted to study the behavior of domain patterns. Finally, there are already good algorithms such as Metropolis [94] that has been successfully applied to various problems. A literature review about Monte Carlo simulation on ferroelectric domains will be followed in chapter 5.

1.9 Layout of this thesis

In chapter 2, evolution of the domain structure in PZT during electrical poling is studied using PFM. For this study, a statistical analysis of PFM data, called piezohistogram analysis, and *ex situ* observation of ferroelectric domains were carried out. A distinct difference in piezohistogram from almost unpoled and strongly poled regions was found. However, the statistical approach does not reveal the evolution of individual domain patterns. To explore this further, domain evolution processes in low-energy domain configuration such as herringbone and checkerboard pattern were observed using VPFM

and a stepwise poling process. The data of crystal orientation from EBSD and compatibility theory were used to assist the identification of polarization directions.

Chapter 3 presents ferroelastic domain evolution under compressive stress loading in PZT, studied using VPFM. The PFM images show several evolution processes of ferroelastic domain structures such as overwriting of one lamellation by a differently oriented lamellation. Using EBSD and PFM data, it was confirmed that switching processes are significantly constrained by pre-existing domain structures, such that the process is mainly one of pattern evolution. The observations are discussed in the context of models of ferroelectric/ferroelastic switching.

In chapter 4, AR-PFM was developed and used in conjunction with EBSD to study ferroelectric domain structure in PZT. The details of AR-PFM including experimental method, the process to generate AR-PFM maps, and the interpretation of AR-PFM map are introduced, using domain patterns observed in PZT. Domain structures were mapped using AR-PFM data, and it is shown that the maps reveal features not seen in other PFM methods. Additionally, using suitable domain patterns, AR-PFM enabled discrimination between the tetragonal and rhombohedral phases at the sub-grain scale.

Chapter 5 presents the development of a Monte Carlo simulation for studying domain evolution. A simplified two-dimensional (2D) model of domain patterns is used. Model parameters are then selected to produce behaviour similar to PZT in that 180° and non-180° domains form. Domain patterns that naturally form to minimize the total free energy are presented. The evolution processes of specific non-180° domain patterns caused by electric field and mechanical stress are also presented. The simulation results are consistent with the experiments in that polarization switching takes place *via* domain wall motions, and domain evolutions are constrained by pre-existing domain patterns. In this chapter, the validity of Monte Carlo method to study ferroelectric domain evolution

is tested. It is found that the model can produce realistic (though simplified) patterns of domain evolution.

Finally, chapter 6 discusses the overall contents of the thesis, and makes a conclusion. It also presents potential research subjects for future work.

Chapter 2. A piezoresponse force microscopy study of ferroelectric domain evolution under electrical loading

In this chapter, evolution of the ferroelectric domains in near-morphotropic PZT was studied using PFM through two distinct methods. In the first method, histograms of pixel intensity were obtained from regions of the same sample that experienced a wide range of electric field intensity. The resulting histograms show a distinct difference in the pattern of piezoresponse signal between poled and unpoled areas. In the second method, poling was conducted on PZT in a series of steps, interrupted by PFM scans, which were used to identify the domain evolution processes. The mechanisms of evolution in low-energy domain configurations such as herringbone structures are studied. Methods are developed for identifying the polarization directions of the individual domains. The methods combine a knowledge of the compatible domain configurations with crystallographic data from EBSD and PFM data. The resulting map of polarization directions enables clear identification of the polarization switching mechanisms. The research presented in this chapter was published as follows:

Kim KL, Huber JE. Observation of the poling process in ferroelectric ceramics using piezoresponse force microscopy. ASME 2012 Conf. Smart Mater. Adapt. Struct. Intell. Syst., Stone Mountain, Georgia, USA: 2012, p. 155–60.

Kim KL, Tsou NT, Huber JE. Domain evolution processes during poling of a near-morphotropic Pb(Zr, Ti)O_3 ceramic. J Appl Phys 2013;113:194104–1–11.

2.1 Introduction and literature review

With the development of characterization techniques, there has been progress in understanding domain wall motion under electric field [30,34,55,61,62,95,96]. In general, both 180° and non-180° domain switching can be induced by electrical loading, and can orient the polarization direction toward an applied electric field. Consequently, non-180° domain structures, such as lamellar structures or needle-like structures, with a favourable polarization direction relative to the applied electric field tend to grow, while those with unfavourable polar direction retreat or disappear. However, most studies to date concern simple domain patterns, and there remain significant gaps in the understanding of switching mechanisms in the more complex domain patterns such as herringbone and checkerboard pattern, composed of both 180° and non-180° domain boundaries, that are commonly observed in bulk ferroelectrics. Figures 2.1(a) and (b) show typical herringbone and checkerboard domain patterns observed from PFM and AFM, respectively. The herringbone pattern in figure 2.1(a) consists of four in-plane polarization directions in tetragonal. And the checkerboard pattern in figure 2.1(b) consists of non-180° domain walls intersected by 180° domain walls. Note that figure 2.1(b) shows the etched surface of single crystal barium titanate. The etchant reacts with *c*+, *c*− and *a* domains at different speeds, and hence the checkerboard pattern is clearly exposed [97]. In the present work, PFM is used to study the evolution of domain patterns in a bulk ferroelectric ceramic.

PFM has significantly contributed to the observation of domains due to its simple operational principle and high spatial resolution [42]. Scanning probe methods have also been exploited in writing domain patterns [98,99]. A current area of research interest is to go beyond establishing the domain configuration and attempt to understand the domain evolution processes when electric fields are applied. Characterization using PFM

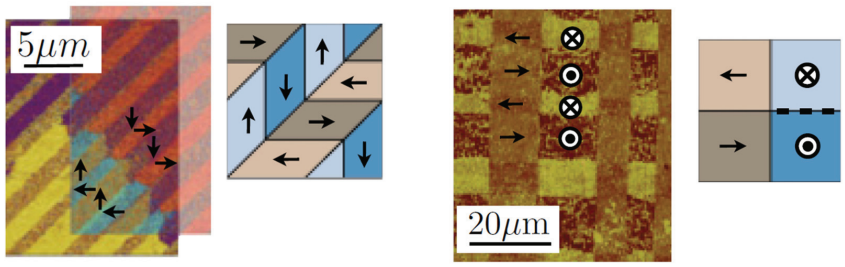

(a) (b)

Figure 2.1: (a) Herringbone domain pattern observed using lateral PFM. (b) Checkerboard domain pattern observed using AFM after etching the surface. Both images were obtained from single crystal barium titanate (modified from [21]).

provides various merits, but it is disadvantageous for *in situ* observation due to its imaging mechanism, which has limited time resolution and can be affected or damaged by strong electric fields. The limited time resolution has been improved by scanning without feedback [52], but this method is inapplicable to imaging the evolution process in bulk PZT, in which the surface has normally some topography features including triple junctions of grain boundary (GB). Thus novel experimental methods using PFM are necessary to study surface domain evolution processes in bulk materials.

In this chapter, the evolution processes of non-180° domain structures in bulk polycrystalline PZT are studied during poling *via* two different experimental methods. First, a change in domain structure during poling is observed statistically through changes in the histogram of piezoresponse intensities in the PFM image. This is achieved through a single application of electric potential difference to a trapezoidal material sample whose shape induces variation in local electric field strength. PFM measurements are made at various points on the sample surface. This method provides statistical information about how varying the electric field strength changes the domain structure. Note that this statistical analysis method using PFM signals is called a "piezohistogram" in some literature [100–102], and has been used to study the effect of capacitor size on the uniformity of switching behaviour [102], the effect of compositional ratio between Zr and Ti ions in PZT films on the population of polarization directions [101], and the local self-

polarization in BFCO film [100]. However, it does not track the detailed evolution of domain structure in any single region.

In order to observe domain evolution, a second experiment was carried out *via ex situ* PFM observation on a polished ceramic surface after applying electric field parallel to the observation plane. This allows observation of switching processes during an interrupted ceramic poling operation. Poling was carried out step-by-step by applying increasing levels of electric field, each step being followed by PFM observation to reveal changes in domain pattern.

A key feature of the second method is the identification of polarization directions in three dimensions by utilizing a combination of PFM data, crystallographic orientation data from EBSD, the compatibility of low energy microstructure configurations, and the effects of applied fields on domain evolution. Prior studies to identify polarization directions in three dimensions were achieved by combining VPFM and LPFM data [79,80]. However, this method presents particular difficulty in near-morphotropic PZT because of the coexistence of the rhombohedral and tetragonal phases [15,16]. This gives 14 possible polarization orientations and complicates the relationship between the piezoelectric response and the polarization vector. In this chapter, mapping of polarization directions in three dimensions is achieved by exploiting the fact that non-180° domain walls form in the {100} and {110} planes in PZT. Using local crystallographic orientation data from EBSD, the domain wall orientations in the PFM images are identified among the crystallographic planes of the set of possible domain walls [80]. Ambiguity among the resulting interpretations of domain pattern is resolved by use of compatibility relationships [21] such as the head-to-tail polarization relationship [34,56] and recognizing the effect of electric field in aligning polarization [61,103]. This method reveals distinct mechanisms of domain evolution, including the evolution of herringbone-

type structure by growth of lamellae to overwrite adjacent regions, lengthening of lamellae without broadening, and simultaneous lengthening and broadening of non-180° lamellae intersected by 180° domain walls.

2.2 Piezohistogram – Experimental method

An isosceles trapezoidal-shaped PZT specimen was designed such that a single application of electric potential difference would produce a range of field strengths between 0.5 MVm^{-1} and 2.5 MVm^{-1}. Figure 2.2 shows a simulation of electric field values in the specimen during poling. This simulation was conducted using the PDE toolbox in Matlab. In the isosceles trapezoid, two electrodes are placed on the right and the left sides while the top and bottom sides are insulated. In the PDE toolbox, the boundary condition can be specified via either the Dirichlet or the Neumann method. In the Dirichlet boundary condition, the electric potential φ is specified on the boundary. Meanwhile, the insulating boundary condition in the Neumann method is given as $\mathbf{n}\cdot(\nabla\varphi)=0$ where $\mathbf{n}$ denotes the normal vector to the boundary. Thus, Dirichlet and Neumann boundary conditions were applied to the electrodes and the insulating sides, respectively. Note, the simulation is based on linear dielectric response and neglects the detailed effects of nonlinearity due to ferroelectric switching. Thus the governing equation solved was simply $\nabla^2\varphi=0$. Consequently the field levels reported are approximate. The experiment was designed to compare domain structures between almost unpoled and fully poled areas by collecting data from several different areas and applying statistical analysis.

A near MPB composition of soft PZT, designated PZT-855 and distributed by APC International, was used. The bulk polycrystalline PZT was provided in the unpoled

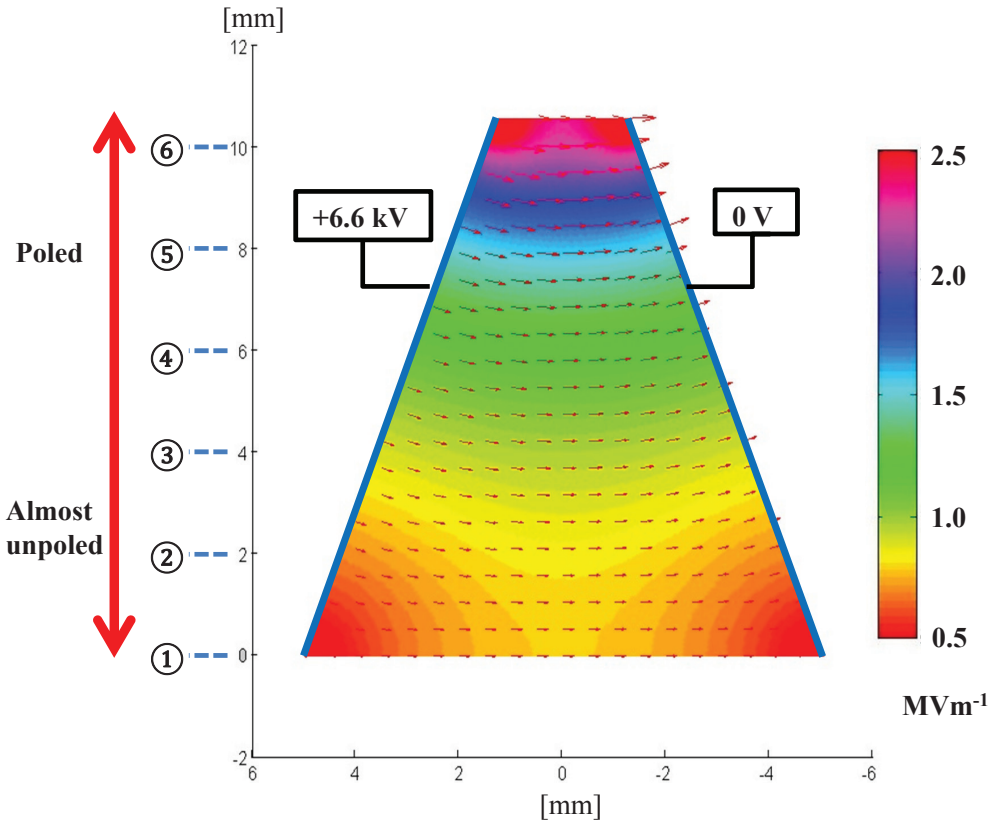

Figure 2.2: Simulated electric field in the PZT specimen. PFM scanning was conducted at points near each line 1–6.

state with typical grain size 2–5 μm. A plate of thickness 0.55 mm was cut out in a trapezoidal shape using a precision diamond saw, with base 10 mm, height 10.55 mm and upper edge length 2.5 mm as shown in figure 2.2. One side of the specimen was polished to a mirror finish using a suspension of colloidal silica of 40 nm grain size. To apply electric field to the specimen, conductive electrodes were formed and wires were connected to the sloping sides using conductive epoxy resin. An electric potential of 6.6 kV was applied for 20 seconds and a Sawyer-Tower circuit [97,104] was used to monitor charge on the electrodes. The resulting electric field strength ranges from about 0.5 MVm^{-1} to 2.5 MVm^{-1} on the specimen, while the coercive field of PZT-855 is close to 0.85 MVm^{-1}. Thus the area close to the base of the trapezium was almost unpoled while the area near the upper edge was fully poled.

After poling, the specimen was mounted on a conductive metal plate using silver paint to ground the specimen for PFM measurement. VPFM scanning was conducted in air at room temperature using a Veeco Dimension 3100 nanoscope atomic force microscope, with simultaneous PFM and topography measurement. Bruker SCM-PIC probes were used with a scan rate and scan resolution of 1.49 Hz and 512 samples/line, respectively. A 3–5 V amplitude of tip voltage, at 200 kHz frequency was used. Scans of varying size, 10 μm × 10 μm up to 25 μm × 25 μm were made. Since typical domain feature sizes in the scans were 50 nm (lamellar bands) up to about 2 μm (180° watermark patterns), each scan contained a sufficient number of domains to allow for statistical measures to be calculated. Note that the poling direction was in-plane, while the VPFM measurements detect variation in out-of-plane piezoelectric response. PFM scanning was performed on three areas for each of the 6 lines indicated on figure 2.2. Since topographic cross talk can affect PFM data the scanning areas were chosen so as to avoid topographic features, maintaining flatness to within about 200 nm.

2.3 Piezohistogram – Result

Typical PFM images contained 512 × 512 samples, giving 262,144 events, from which histograms of event counts were constructed. The distribution of piezoresponse signal was divided into 3,000 intervals, and truncated at the extremes of piezoresponse to remove the long tails of the distribution which mainly correspond to noise. Figure 2.3 shows normalized histograms taken from near each of the lines indicated in figure 2.2. The approximate field strength experienced in the region ±500 μm from each line is shown.

In each histogram, one or more peaks can be observed, indicating frequently

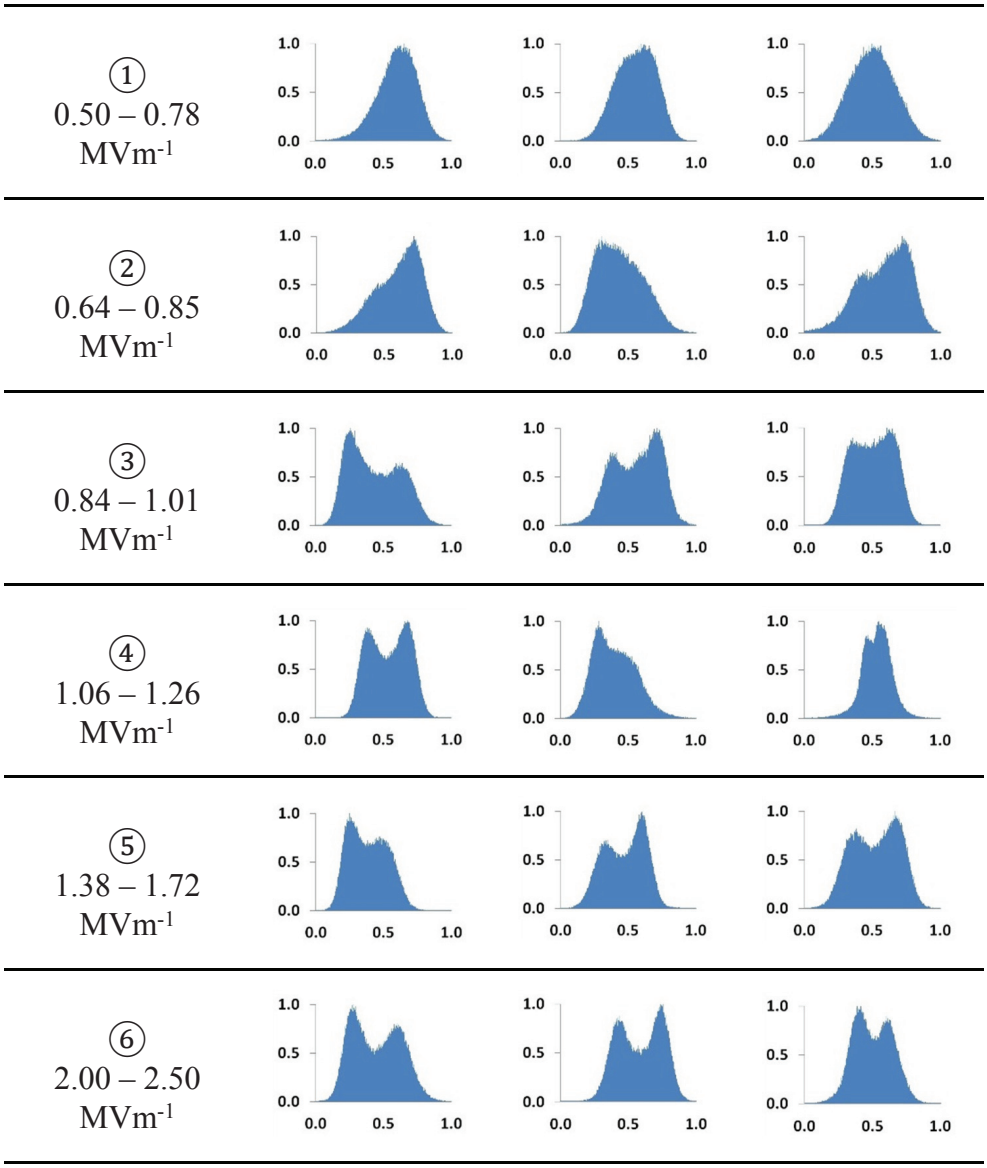

Figure 2.3: Histograms showing normalized event counts versus normalized value of piezoresponse signal corresponding to regions near each line marked in figure 2.2.

occurring values of piezoresponse. However, the histograms can generally be categorized into one of two types based on the number of major peaks: M-shaped distributions show two clear major peaks, while dome shaped distributions have a single major peak. Some of the distributions are skewed negatively or positively indicating a dominant piezoresponse signal but with a second strong signal present. The measurements do not

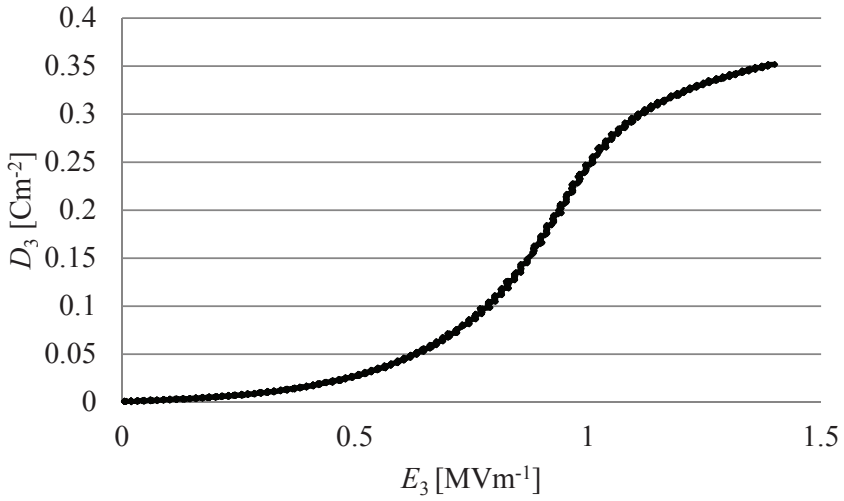

Figure 2.4: Measured electric displacement (D_3) versus electric field (E_3).

indicate with certainty a dominant surface polarization direction because frequency-dependent contrast reversal often occurred [105].

Comparing histograms taken from line 1, ($0.5-0.78$ MVm^{-1}) with those taken from line 6 ($2.0-2.5$ MVm^{-1}) it is immediately evident that dome-shaped histograms dominate the scans of the unpoled material while M-shaped histograms occur in strongly poled material. In fact, M-shaped histograms dominate the response from about line 4 onwards. This is consistent with a transition at about 1.0 MVm^{-1} from dome to M-shaped histograms. In terms of the poling of the ceramic, the majority of polarization change during the poling process occurs before the field strength reaches 1.0 MVm^{-1} (see figure 2.4), so the statistical change in the measurements is not directly linked to macroscopic polarization. Instead, field strengths above 1.0 MVm^{-1} correspond to the portion of the dielectric hysteresis in which the dielectric response becomes saturated.

2.4 Piezohistogram – Discussion

Histograms taken from a pair of regions near line 1 ($0.5 - 0.78$ MVm^{-1}) and line 6 ($2.0 - 2.5$ MVm^{-1}) are shown alongside the corresponding PFM images in figures 2.5(a) and (b), respectively. This demonstrates how the histograms are related to the observed domain structure. In figure 2.5(a), lamellar structures (non-180° domain walls) as well as watermark patterns (180° domain walls) can be observed. Occasionally the domain structures contain both 180° and non-180° domain walls, with the 180° domain walls windingly traversing the lamellar structures. By contrast, the domain structure observed from line 6, figure 2.5(b), consists of only watermark-type pattern, with no lamellar structure. It can be observed that the watermark pattern produces an M-shaped histogram due to the presence of two sharply distinct polarization states. However, the presence of non-180° domain boundaries typically produces regions of intermediate contrast that result in the disappearance of a clear distinction between positively and negatively polarized states in the histogram. In such cases the greatest number of events generally occurs near the central area of the histogram. Simplistically, the dome-shaped histogram identifies the presence of a significant region of lamellae while an M-shaped histogram identifies 180° watermark domains. In practice, most unpoled regions consist of a mixture of lamellar and watermark domains.

The correlation between histogram shape and domain structure suggested by figure 2.5 can be understood by considering the scale of the domain structure relative to the size of the probe-tip. It has been shown that the electric field strength in PFM applications decreases sharply in the sample material with distance from the tip [106]. Thus the sample volume contributing to the piezoresponse signal has a limited size of order several times the tip radius. In the present experiment a typical tip radius of about 20 nm was used. As shown in figure 2.6(a), coarse domains such as the 180° domain

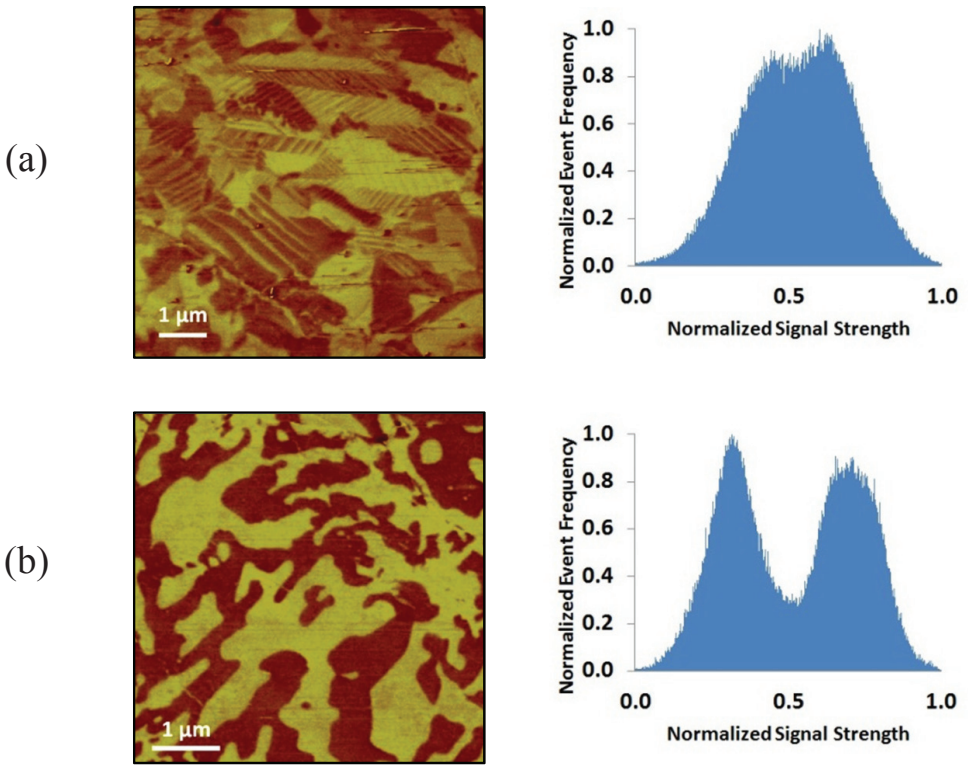

Figure 2.5: VPFM images and their histograms. (a) taken from near line 1, and (b) from near line 6 of figure 2.2.

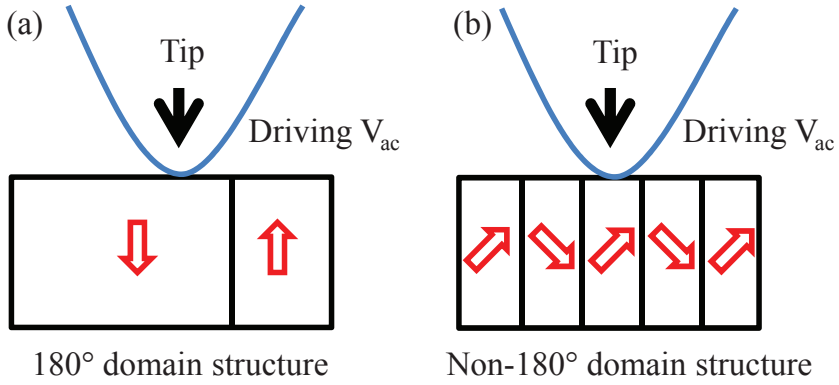

Figure 2.6: Piezoresponse signal intensity from domains is significantly different when the tip scans coarse 180° domain structures and fine non-180° domain structures.

watermark patterns are expected to contribute a strong signal contrast between domains. Conversely, fine domain patterns such as the lamellar non-180° structures of figure 2.5(a) have domain spacing comparable to the size of the sampled volume. Consequently the piezoresponse signal may contain contributions from several domains excited by the tip resulting in an intermediate signal value. The finest lamellar structure which can be

observed from figure 2.5(a) consists of approximately 50 nm thick alternating domains. Given a 20 nm tip radius, lamellae finer than this may not be resolved, resulting in fuzzy image regions.

The marked change in domain structure between the poled and unpoled areas is likely to be caused by domain evolution during poling. In particular, non-180° domain structures are much less prevalent in the PFM images from line 6 where the strongest electric field was applied, consistent with the idea that the extinction of non-180° domain structure occurred in these areas during poling. However, since the observations in figure 2.5 come from different areas of the sample, they do not provide direct evidence of domain evolution processes. Examination of numerous PFM images showed that both 180° and non-180° domain structures are normally observed at the surface of an unpoled PZT specimen. Thus, the watermark pattern at line 6 might conceivably have been present before the electric field was applied. Furthermore, the histograms do not reflect any information about the spatial relationship between the sampled points but only count the number of similar events over the whole imaging area. Therefore, further work was carried out to observe domain structure evolution more directly.

2.5 *Ex situ* observation – Experimental method

The same material PZT-855 was cut into sample of size $3\times5\times0.5$ mm^3. One 3×5 mm^2 side of the specimen was polished using the same method introduced in section 2.2. To apply electric field, electrodes were formed on the 5×0.5 mm^2 faces using conductive epoxy resin. A modified Sawyer-Tower circuit was used for monitoring surface charge on the electrodes. Electric field, was applied as shown in figure 2.7(a), with amplitude $\alpha = 0.5,\ 0.75,\ 0.9,\ 1.4$ and 1.9 MVm^{-1}. Figure 2.7(b) shows the recorded electric

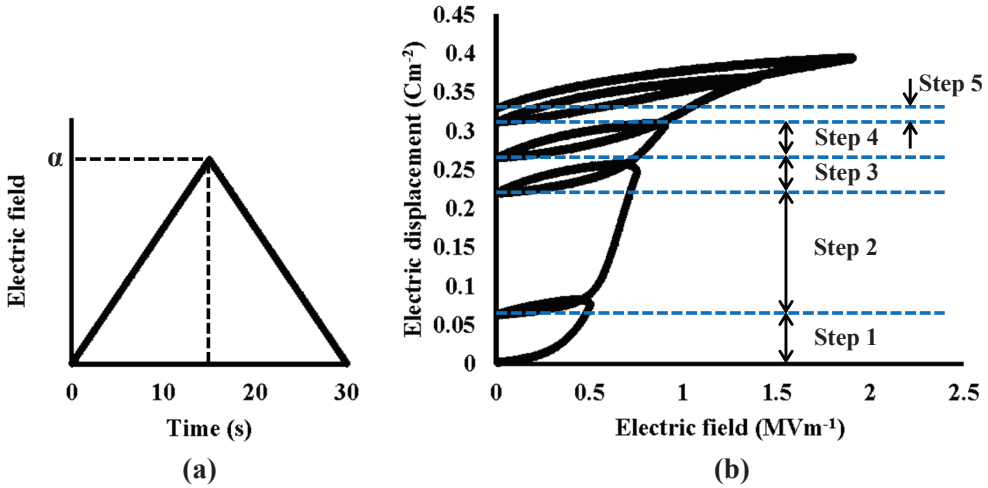

Figure 2.7: (a) Applied electric field signal pattern. (b) Electric displacement versus electric field during five poling steps.

displacement versus electric field, corresponding to the series of five loading and unloading steps. Figure 2.7(b) is corrected for current leakage which gave 0.024 Cm^{-2} additional charge in the electrometer over the duration of the experiment. All experimentation was carried out at room temperature.

After each step, the specimen was adhered to a steel mounting disc using conductive paint to ground the specimen for PFM measurement. The experimental configuration was such that the direction of applied electric field was parallel to the PFM image plane, see figure 2.8. VPFM scanning of 10×10 μm^2 regions was conducted using a Veeco Dimension 3100 nanoscope. In this instrument, the PFM signal contains mixed amplitude and phase data, as discussed in chapter 1 and appendix A.1. Bruker SCM-PIC probes were used with a 3–5 V amplitude of tip voltage, at 150–200 kHz. The PFM cantilever was frequently refreshed throughout to avoid artefacts due to tip degradation. The direction of applied electric field was from left to right relative to each PFM image.

To obtain crystallographic orientations, EBSD was conducted using an Evo LS 15 environmental scanning electron microscope (ESEM), operating at 10 Pa pressure and 10–15 kV. The resulting Kikuchi patterns were analyzed *via* Hough transforms using

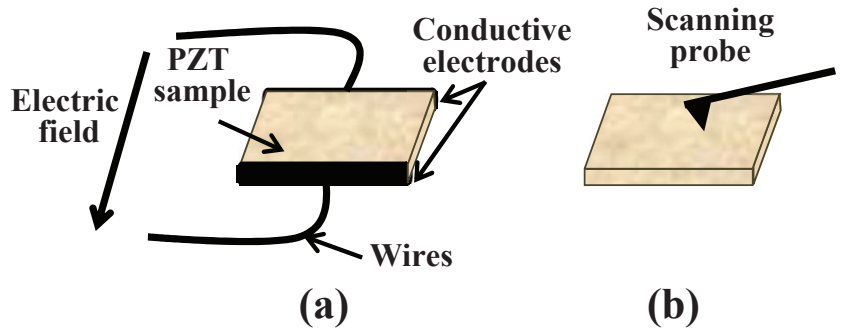

Figure 2.8: Schematic of (a) poling step, (b) *ex situ* scanning after poling step.

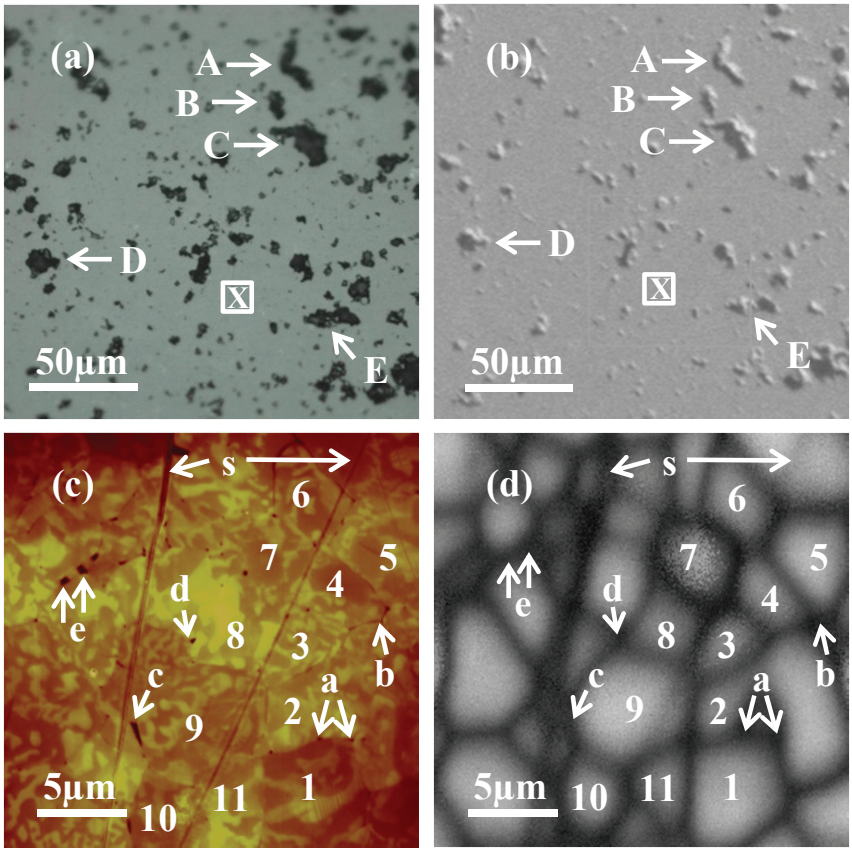

Figure 2.9: PFM imaging area, marked 'X' was traced *via* (a) optical image and (b) SEM image. (c) AFM topography image in region X, and (d) EBSD image quality map in region X.

Orientation Imaging Microscopy data analysis software. To obtain accurate registration between EBSD and PFM measurements, the location was traced using several techniques. Figure 2.9(a) shows an optical image acquired before PFM scanning, and used to identify regions of sample surface clear of significant topographic features such as pores that could interfere with the PFM measurement. The SEM image figure 2.9(b) was taken

before tilting by 70° to collect Kikuchi bands and shows similar features (marked 'A'–'E') to figure 2.9(a). The AFM topography image, figure 2.9(c), PFM images and EBSD data (figure 2.9(d)) were collected from the 10×10 μm^2 region 'X' in figures 2.9(a) and (b). Accurate registration was confirmed by identifying common features such as pores at triple junctions and ceramic grains in the AFM topography image and EBSD image quality map, see labels a–e and 1–11 in figure 2.9. Polishing scratch lines marked 's' can also be observed at matching locations in figures 2.9(c) and (d).

2.6 *Ex situ* observation – Identification of polarization directions

2.6.1 Identification methods

The interpretation of PFM images taken from a surface in near-morphotropic PZT entails a number of challenges. Aside from effects that may influence the PFM signal [42,75], there is significant difficulty in determining the polarization direction from the vertical piezoelectric response. Note that in this material the tetragonal and rhombohedral ferroelectric phases can coexist. The co-existence of tetragonal and rhombohedral phases allows for 14 distinct polarization orientations and since the sample is a randomly oriented polycrystal, there is no certainty over polarization direction from VPFM data alone. The EBSD data provides crystallographic orientation but was not sufficiently precise to discriminate the phases, because of the subtle nature of the structural transition at the MPB. Identification is further complicated by the relationship between crystal orientation and the surface normal piezoelectric coefficient, which does not give a unique interpretation of polarization state from a measurement of vertical piezoelectric response alone [78,107,108]. The use of carefully calibrated three-dimensional PFM [109,110] can

go some way towards reducing ambiguity in the PFM data, but even with this method, there remains uncertainty when more than one phase may be present, or when the nano-scale piezoelectric coefficients are not well characterised, as is the case here. A significant advantage can be gained when multiple domains are present within one grain. In particular, non-180° domain walls are commonly generated under electrical and mechanical compatibility conditions [19,20], giving specific crystallographic planes, and hence straight lines in the viewing plane. Furthermore, in groups of several domains, the compatibility conditions give rise to a limited set of patterns [21]. Exploiting these conditions provides a unique interpretation, except for certain special cases of alignment between the crystallographic axes and the viewing plane.

To identify polarization directions in a domain structure from the PFM and EBSD data, four distinct methods were employed. Method 1 relies on the observation that the polarization vector lies in the <100> directions in tetragonal and <111> in rhombohedral crystal structure. This results in compatible orientations of non-180° domain walls that are {110} planes in tetragonal crystals and {100} or {110} in rhombohedral crystals, as shown in figure 1.4. Therefore, 9 crystallographic planes of non-180° domain walls can be present in the PZT at the MPB. Let $\mathbf{n}_{\mathrm{d}}'$ be the normal vector of any of the {110} and {100} crystallographic planes in local crystallographic coordinates, and $\boldsymbol{R}$ be a rotation matrix from crystallographic coordinates to instrument coordinates, given by [111]

$$\boldsymbol{R}=\begin{bmatrix} \cos\varphi_1\cos\varphi_2-\cos\Phi\sin\varphi_1\sin\varphi_2 & \cos\varphi_2\sin\varphi_1+\cos\varphi_1\cos\Phi\sin\varphi_2 & \sin\varphi_2\sin\Phi \\ -\cos\varphi_1\sin\varphi_2-\cos\varphi_2\cos\Phi\sin\varphi_1 & \cos\varphi_1\cos\varphi_2\cos\Phi-\sin\varphi_1\sin\varphi_2 & \cos\varphi_2\sin\Phi \\ \sin\varphi_1\sin\Phi & -\cos\varphi_1\sin\Phi & \cos\Phi \end{bmatrix}, \quad (2.1)$$

where $(\varphi_1,\Phi,\varphi_2)$ are Euler angles. Figure 2.10 shows the three rotations defined by Euler angles. The normal to the viewing plane $\mathbf{n}_{\mathrm{v}}$ is given by $\begin{bmatrix}0 & 0 & 1\end{bmatrix}^{\mathrm{T}}$ in instrument

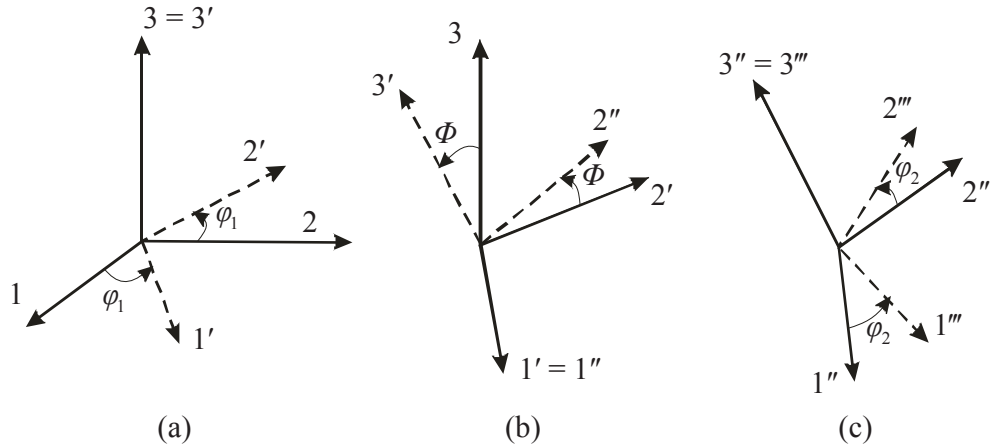

Figure 2.10: Coordinate transformations by three Euler angles $(\varphi_1, \Phi, \varphi_2)$. Counterclockwise rotations are carried out *via* (a), (b), and (c) [75].

coordinates. Then $\mathbf{v}_w = \mathbf{n}_v \times \boldsymbol{R}\mathbf{n}'_d$ is the vector direction of the corresponding domain wall as it appears in the viewing plane. Now taking $\mathbf{v}_{ob}$ as the vector direction of any domain wall observed in the viewing plane, an angular error between the observed wall orientation and any of the habit planes of non-180° domain walls is given by:

$$\theta_{err} = \arccos \frac{\left|\mathbf{v}_w \cdot \mathbf{v}_{ob}\right|}{\left|\mathbf{v}_w\right|\left|\mathbf{v}_{ob}\right|}. \tag{2.2}$$

Allowing for angular errors due to accuracy of the EBSD data (±2°), misalignment between instruments (±2°), and deviations from the compatible domain wall orientation (±2°), for example in wedge-shaped domains, suggests an angular tolerance of about ±6°. Any domain wall with $\theta_{err} < 6°$ was taken to be a possible interpretation of a straight interface observed in the PFM data.

Method 1, above, leaves ambiguity in the identification of polarization directions for several reasons: Depending on the crystallographic orientation, it may be that several domain wall orientations $\mathbf{n}'_d$ meet the criterion $\theta_{err} < 6°$. Furthermore, the {110} walls are common to both the rhombohedral and tetragonal systems. Finally, reversal of the polarization vector on both sides of a domain wall is possible without affecting the

domain wall orientation. Therefore further methods are needed to identify polarization unambiguously.

A second method uses line profiles from the PFM signal to identify the phase state or polarization direction. Method 2 can be used after method 1, to discriminate among several interpretations of the polarization states that are consistent with the known domain wall orientations. A PFM line profile taken across several domains can then indicate the relative signal strength and sign for these domains. Configurations that are inconsistent with the result of the line scan can be eliminated.

Interpretation of PFM line profile data has previously been discussed in the context of thin films by Ganpule *et al.* [112,113]. However, because the domain spacing is only a few times the tip radius in our study, and also due to the complex orientational dependencies of the piezoelectric effect, a detailed interpretation of the line profile data was not practical and instead we use the line profile merely to discriminate between strongly distinct polarization states. An example is to discriminate between the tetragonal and rhombohedral phases because of their differing polarization directions and hence differing PFM signals. Another example is differentiating domains with an in-plane polar direction (weak signal) from those with an out-of-plane polar direction (strong signal) in the tetragonal phase. This latter example is often applicable because it is common for at least one tetragonal polarization direction to lie within about 10° of the viewing plane. In the rhombohedral phase, a domain with in-plane polarization may still give a strong VPFM signal. This arises because the orientation of maximum piezoelectric response is not aligned to the polarization vector [78,107,108]. Note that identification of the phase or polarization state using the PFM signal from a single domain is unreliable because of effects due to contrast reversal, signal calibration and background noise [42]. Generally

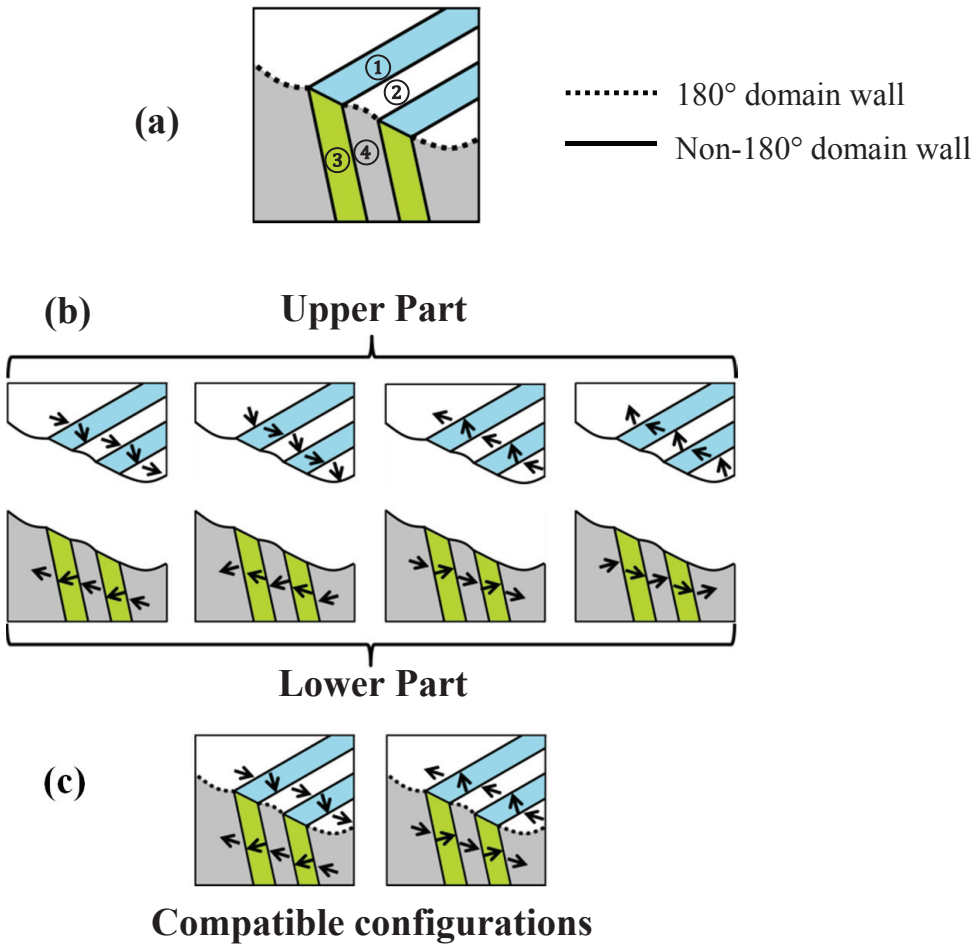

Figure 2.11: (a) A schematic of rank-2 herringbone-like domain structure with four domains 1 – 4. (b) Four possible arrangements of polarization directions in each of the upper and lower parts of the domain structure in (a). (c) Two compatible configurations.

comparison of signal across several domains provides greater reliability. A detailed example of method 2 will be described in section 2.6.2.

A third identification method exploits the limited possibilities for arrangement of groups of four domains under compatibility conditions. A typical example of method 3 is illustrated in figure 2.11(a). This structure can be thought of as two lamellar regions meeting at a common boundary. Suppose that method 1 and 2 have been applied, and give rise to four distinct interpretations for each lamellar region – see figure 2.11(b). Now applying compatibility conditions to the junctions between the two lamellar regions further limits the possible interpretations. In figure 2.11(c) only two ways of pairing the

laminations satisfy compatibility requirements, because polarization vectors must be antiparallel across 180° domain walls (dotted line).

Methods 1–3 may still leave ambiguity over the sign of the polarization vector. However, in the present work the evolution of the domain pattern is observed as the applied electric field strength is increased. In method 4, polarization switching is expected to align the polarization direction towards the applied electric field. Thus, by observing the evolution of the domain pattern, a hypothesis about specific polarization directions can be made [61,103]. This fourth method is particularly useful when identifying the polarization vector in a growing domain or a retreating domain within a 180° domain pattern. Given polarization vector **p** and applied electric field vector **E**, the angular difference, $\theta_{\mathbf{p},\mathbf{E}} = \arccos(\mathbf{p}\cdot\mathbf{E}/|\mathbf{p}||\mathbf{E}|)$ is expected to be less than 90° for a growing domain in a 180° domain pattern.

Finally, it is worth noting that in some cases, the combination of phase and crystallographic orientation could still make one or more of the methods used to identify domains difficult to apply. The examples presented here focus on cases where the identification methods allowed an unambiguous discrimination of domains.

2.6.2 Application of the four methods to domain structures in a PFM image

The four methods were applied to identify polarization directions in the domain structures in figure 2.12. Features visible in figure 2.12(a) include both 180° and non-180° domain boundaries. Lamellae, with orientation $\mathbf{v}_{ob1}$ (marked P), and a region of herringbone-like structure (marked Q, see figure 2.12(b) for an enlarged view), composed of two distinct orientations of non-180° domain wall $\mathbf{v}_{ob1}$ and $\mathbf{v}_{ob2}$, appear.

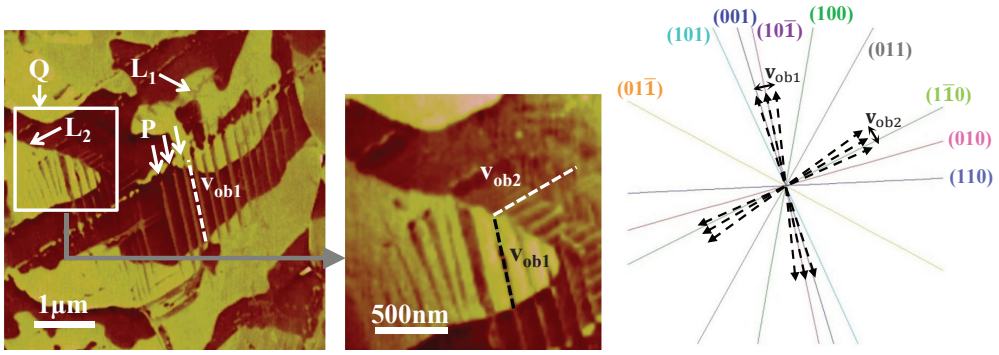

Figure 2.12: Identification of crystallographic planes in PFM images by method 1. (a) A PFM image at unpoled state (b) Enlarged view of region Q. (c) Orientations of {100} and {110} planes and observed domain walls in the viewing plane, showing ±6° tolerances.

Additionally in figure 2.12(a), domains in light contrast L_1 and L_2 that form part of the 180° domain structure are identified.

To begin with, figure 2.12(c) shows all the orientations that can be generated by {100} and {110} planes intersecting the viewing plane after rotation through the Euler angles (197.0°, 78.1°, 354.0°) corresponding to the crystal orientation of the grain in which the domain structures P and Q are present. By comparing the orientations of {110} and {100} planes with the observed non-180° domain walls in figure 2.12(b), method 1 identifies the domain wall orientations as (001) or $(10\bar{1})$ for $\mathbf{v}_{ob1}$, and $(1\bar{1}0)$ for $\mathbf{v}_{ob2}$.

Figure 2.13 shows how method 2 can be applied to identify the phases present and provide more specific information about the domain wall orientations. Using the crystal coordinates of figure 2.13(a), the compatible polarization pairs across non-180° domain walls in the $(10\bar{1})$ and (001) planes are shown in figure 2.13(b). Note that domain walls can be formed in the $(10\bar{1})$ plane in both tetragonal and rhombohedral phases while (001) domain walls are found only in the rhombohedral phase. The possible phases and polarization directions can be distinguished by considering the expected amplitude of PFM signal from each combination.

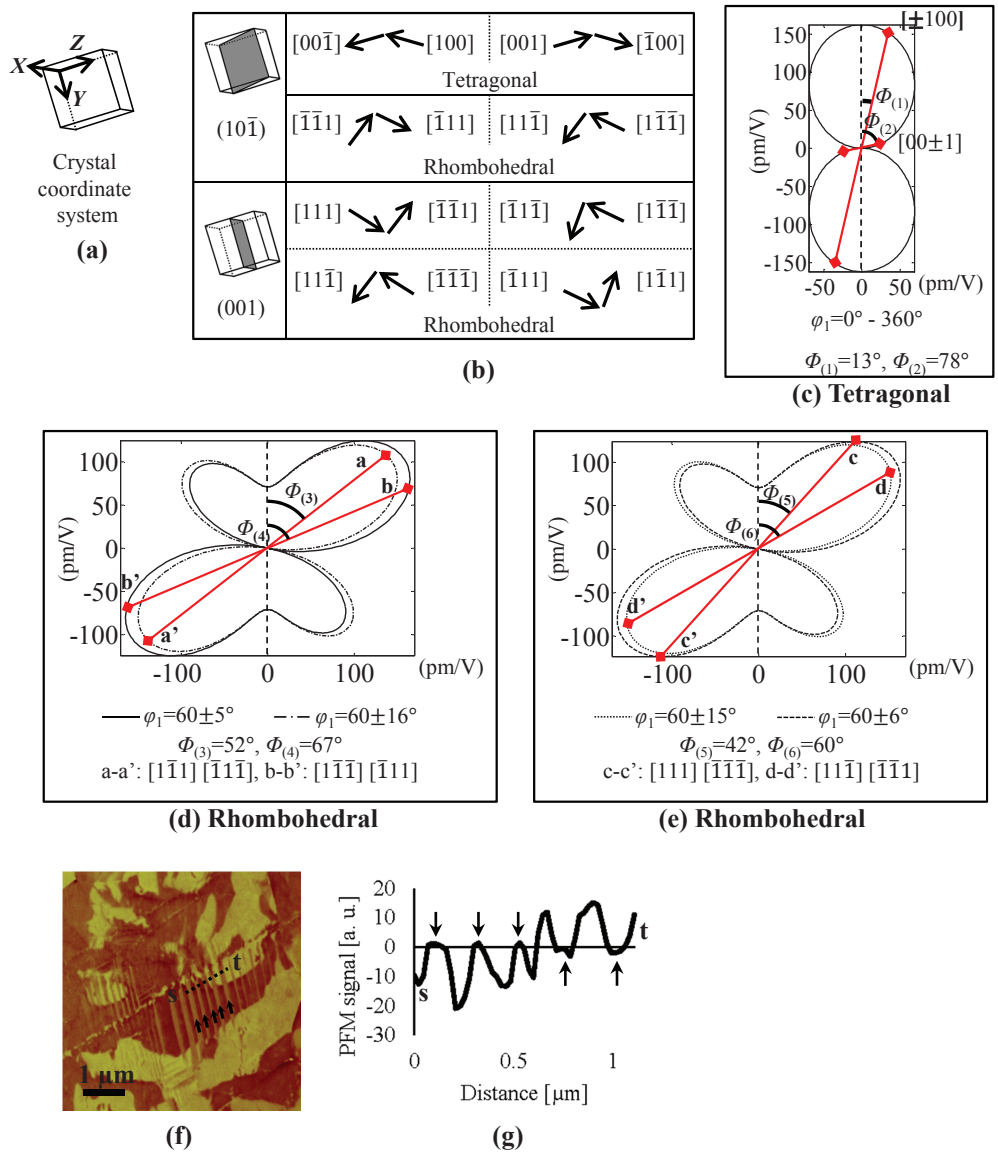

Figure 2.13: Identification of polarization directions using method 2. (a) Crystal coordinate system. (b) Possible polarization directions in head-to-tail relationship for the non-180° domain walls $\mathbf{v}_{ob1}$ in figure 2.12. (c)–(e) The expected magnitudes of d_{zz} for the polarization directions in (b) [78]. (f) PFM image of the region of interest after application of 1.4 MVm^{-1} electric field. (g) PFM line scan along s–t.

Effective piezoelectric coefficient d_{zz} is often used to represent the piezoelectric coefficient contributing to the vertical component of surface displacement from the viewing plane in the instrument coordinate system [79,107]. Figures 2.13(c)–(e) show polar plots of the expected variations in effective piezoelectric coefficient d_{zz} as the angle Φ between the polarization and instrument z-axis is varied. Piezoelectric coefficient data

from Ref. [78] was used; though not identical to our MPB material, this illustrates the effect of polarization direction on d_{zz} – for further details see appendix A.2. and refs [78,99,107,108,114]. From figure 2.13(c), the d_{zz} value due to a tetragonal domain with [00±1] polarization is much smaller than that corresponding to [±100] polarization. By contrast, the magnitudes of d_{zz} in rhombohedral are very close to each other – see figures 2.13(d)–(e). This difference between pairs of d_{zz} values in the two phases can be distinguished using a VPFM line profile. A line profile was taken along s–t in figure 2.13(f), and is shown in figure 2.13(g), with the locations of lamellar bands marked by arrows. Noting that the signal amplitudes drop to near zero in alternate bands identifies these bands with the tetragonal case, and confirms that the domain walls in direction $\mathbf{v}_{ob1}$ are $(10\bar{1})$ domain walls with alternating [±100] and [00±1] polarization directions.

In the herringbone structure of figure 2.12(b), enlarged in figure 2.14, two distinct orientations of non-180° domain bands ($\mathbf{v}_{ob1}$ and $\mathbf{v}_{ob2}$) are present. The region was identified as tetragonal phase material by method 2, and the lines parallel to $\mathbf{v}_{ob1}$ were identified as $(10\bar{1})$ domain walls. Method 3 is next used to identify compatible arrangements of polarization in this region. Only two such arrangements exist, and these are as shown in figures 2.14(b)–(c). In these configurations, the polarization directions are antiparallel across the wavy line which is interpreted as a 180° domain wall, and 90° head-to-tail across all straight boundaries.

Finally, it is noted that the light contrast domains (L_1 and L_2), which were labelled in figure 2.12, gradually disappeared during electrical loading (see figure 2.15 and figure 2.17). Using method 4, these domains in light contrast are expected to have

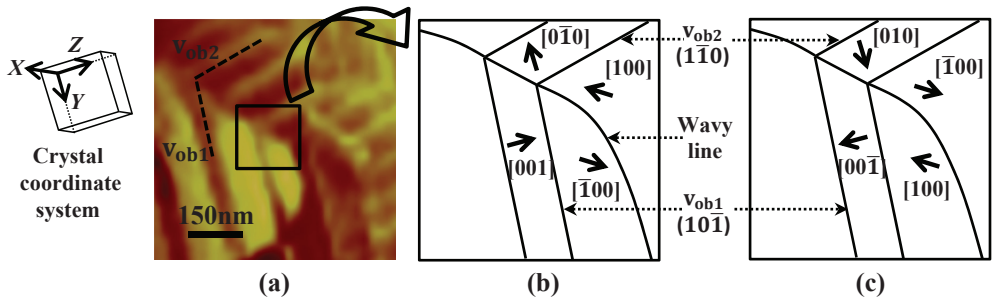

Figure 2.14: Mapping polarization direction through method 3 and 4 for the herringbone-like structure. (a) PFM image. (b)–(c) Maps of compatible polarization directions corresponding to the square in (a).

polarization directions more than 90° away from the applied field direction. This uniquely identifies the polarization directions as those shown in figure 2.14(c).

2.7 *Ex situ* observation – Results and discussion

In this section, 3 examples of the evolution of complex domain patterns under electric field are studied in detail: overwriting of a herringbone-like structure by competing groups of lamellae, broadening of lamellar bands without lengthening, and the simultaneous broadening and lengthening of needle-like domain structure. The non-180° domain structures in the latter two examples are intersected by 180° domain walls forming checkerboard patterns.

2.7.1 Herringbone structure: Competing lamellae and 180° domain switching

In the present study we observe a region of herringbone-like microstructure evolving under steadily increasing electric field. Figure 2.15 shows the evolution of the region of herringbone-like microstructure. Here, one set of lamellae (A_1) grows, and overwrites a

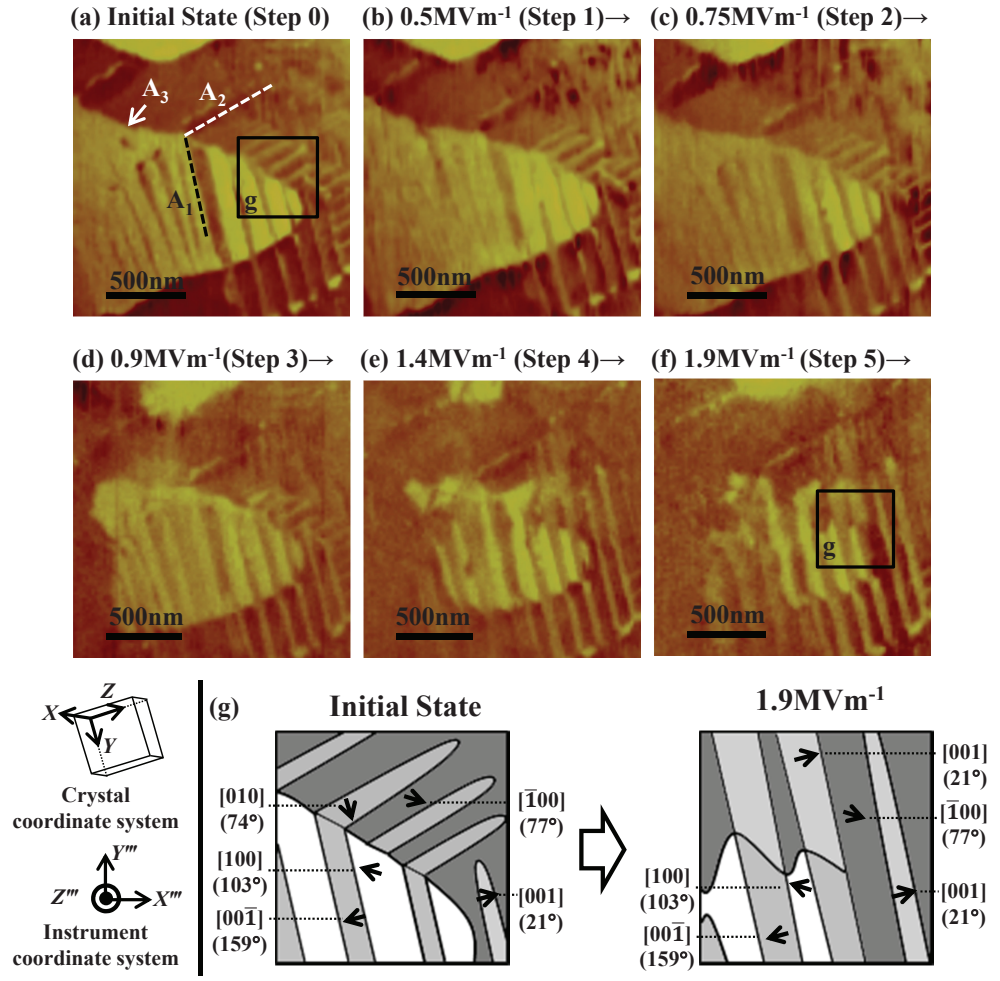

Figure 2.15: (a)–(f) A herringbone-like domain structure evolves into a single lamination during poling. (g) Schematics of region 'g' showing the polarization directions at initial state and after application of 1.9 MVm^{-1}.

second set of lamellae (A_2) that vanishes at the same time. The PFM images corresponding to steps 1–3 (figures 2.15(b)–(d)) show only slight changes in the domain structure, and the herringbone pattern, A_1 and A_2, remains after step 3. After step 4 (figure 2.15(e)), however, the set of lamellae A_2 have vanished, and the lamellae A_1 have started to extend into the region formerly occupied by A_2. Figure 2.15(f) shows that the lamellae A_2 have completely vanished during poling, causing the herringbone-like structure to be replaced with a single lamination. In summary, a herringbone structure was transformed into a single lamination during the electrical loading process. Note that

the 180° domain wall marked A_3 gradually retreats, causing the domain in light contrast to reduce in size.

Figure 2.15(g) shows a reconstructed map of polarization directions for a region of the herringbone-like domain structure, corresponding to the rectangles marked 'g' in figure 2.15(a) and figure 2.15(f). Polarization directions are given in crystal coordinates, while the applied electric field is in the [100] direction in instrument coordinates. The evolution process of the herringbone-like domain structure can be explained by considering the angle between the applied electric field and the polarization direction: $\theta_{\mathbf{p},\mathbf{E}} = \arccos(\mathbf{p}\cdot\mathbf{E}/|\mathbf{p}||\mathbf{E}|)$. This angle is shown for each domain in figure 2.15(g). The $\theta_{\mathbf{p},\mathbf{E}}$ angles of the growing [001] lamellae is 21°, while the shrinking [010] lamellae have, $\theta_{\mathbf{p},\mathbf{E}} = 74°$. Hence the growing lamellae have better alignment of polarization towards the applied electric field. Similarly, the growing lamellae broaden with applied field, absorbing material from the surrounding domain whose $\theta_{\mathbf{p},\mathbf{E}}$ value is 77°. The observation can be summarized as follows. First, in the herringbone-like domain structure composed of two sets of lamellae, the lamellae with the smallest $\theta_{\mathbf{p},\mathbf{E}}$ value overwrite surrounding material. This can happen even when the surrounding material has $\theta_{\mathbf{p},\mathbf{E}} < 90°$ and so is energetically favoured by the electric field. Second, the 180° and 90° domain switching processes are not distinct in time, appearing to occur together as the herringbone structure is rearranged into a single set of lamellae.

It is of interest to relate the patterns of domains in figure 2.15(g) to the families of rank-2 laminations in tetragonal ferroelectrics that can be generated from the constrained theory of compatibility [21]. In the initial state, junctions of 4-domains are seen with successive polarization directions $[100], [00\bar{1}], [010], [\bar{1}00]$ clockwise around the junction. A corresponding pattern of domains can be identified in figure 3 of Tsou *et al*. [21],

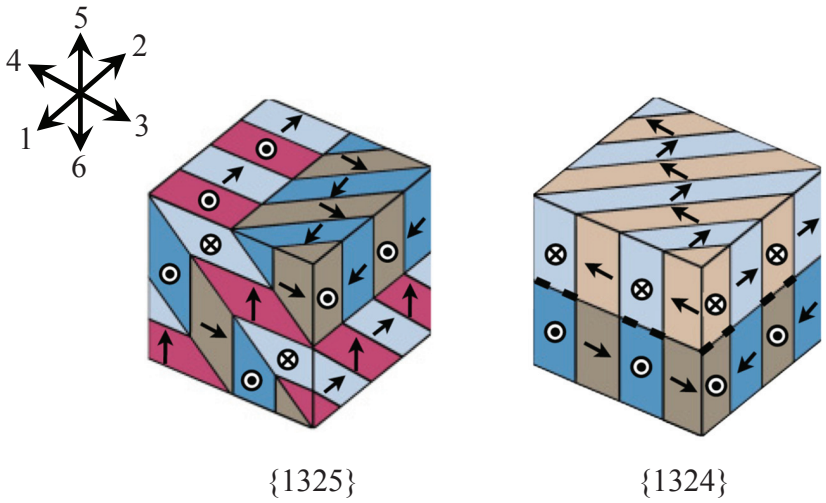

Figure 2.16: {1325} and {1324} families of laminations. The numbers in the brackets indicate polarization directions (modified from [21]).

where the pattern is labelled as the {1325} family of laminations, see figure 2.16. After application of 1.9 MVm^{-1} electric field, we can identify new junctions of 4-domains, now with successive polarization directions $[100],[00\bar{1}],[001],[\bar{1}00]$ working clockwise around the junction. In fact this is almost the same grouping of domains as seen in the initial state, with only the change $[010]\rightarrow[001]$, a simple 90° switch. But this switch changes the domain walls present and consequently the low energy domain wall orientations, requiring a rearrangement of the domain morphology. The final state after application of 1.9 MVm^{-1} field also corresponds to the {1324} family of rank-2 laminations in figure 2.16 [21].

2.7.2 Checkerboard pattern 1: Broadening of lamellar bands without lengthening, and 180° domain switching

Figure 2.17(a) shows various features including lamellar bands (B_1), domains in light contrast (B_2, B_3) and a domains in dark contrast (B_4) forming a pattern similar to

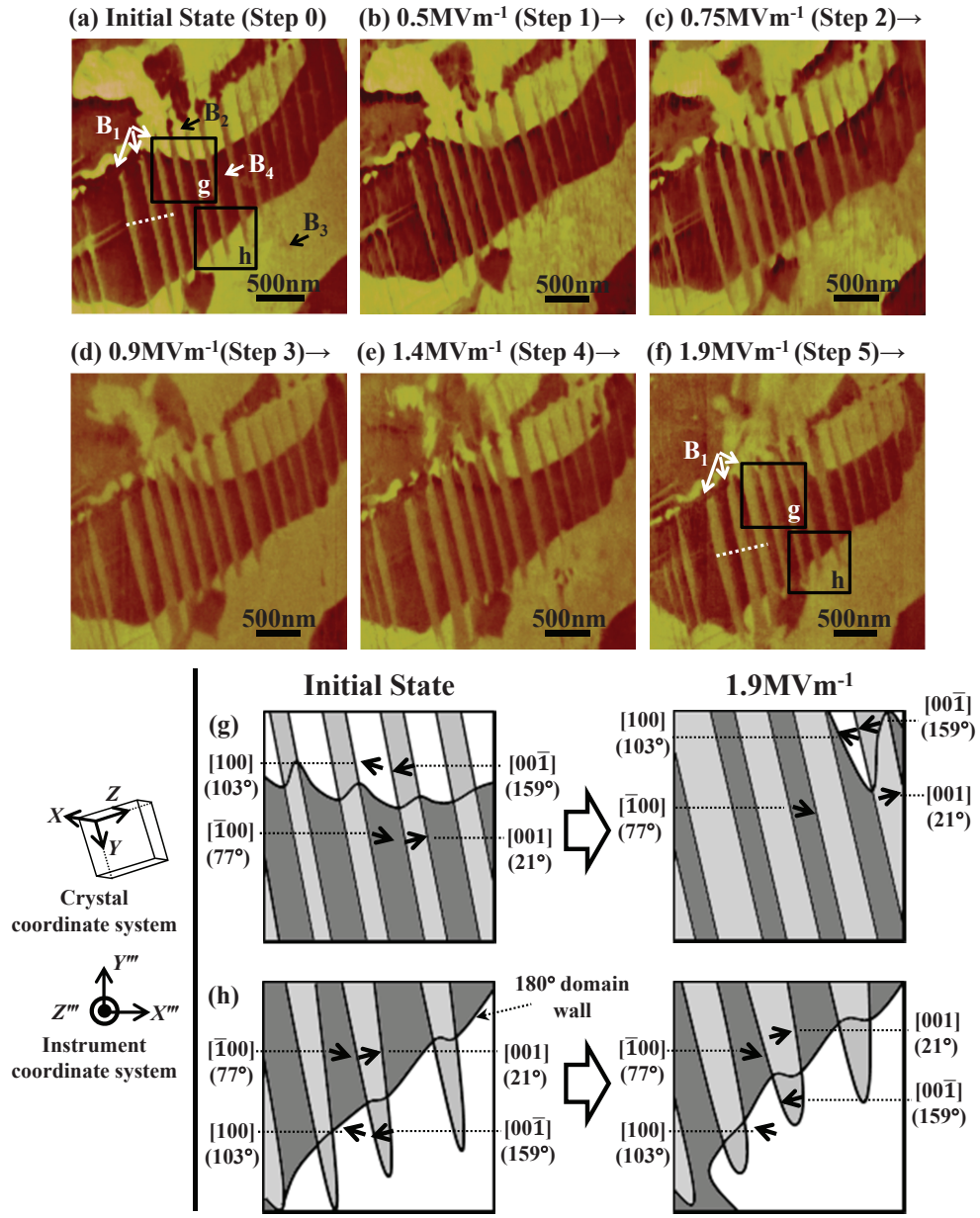

Figure 2.17: (a)–(f) PFM images showing the broadening of lamellae and 180° domain switching during poling. (g)–(h) Schematics of the checkerboard pattern with polarization directions at initial state and after final poling.

checkerboard pattern [21]. From figure 2.17, two distinct domain evolution processes can be seen. To begin with, the thickening of lamellae (B_1) can clearly be observed by comparing figure 2.17(a) with figure 2.17(f). The widths of three lamellae (marked by a dotted line) were measured using a line profile, and their average width increased from

approximately 93 nm to 144 nm during electrical loading. By contrast, there was almost no lengthening of the lamellae in the region of domains B_2 and B_3.

Figures 2.17(g)–(h) shows reconstructed maps of polarization directions for two areas marked 'g' and 'h' in figures 2.17(a) and (f). In figure 2.17(g), broadening of the lamellae occurs by 90° switching from $[\bar{1}00]$ to [001]. During the broadening process, 180° domain wall motion also occurs, causing switching from [100] to $[\bar{1}00]$, and from $[00\bar{1}]$ to [001]. The 180° and 90° domain evolution processes again appear to take place together in a progressive fashion as the electric field strength is increased. In each case switching causes growth of regions of lower angle $\theta_{\mathbf{p},\mathbf{E}}$.

Figure 2.17(h) can be used to explain why the lamellar bands do not lengthen in this case. Lengthening of the lamellae would convert material with $\theta_{\mathbf{p},\mathbf{E}} = 103°$ to domains with $\theta_{\mathbf{p},\mathbf{E}} = 159°$, a process which is not energetically favoured by the applied electric field. It is generally expected that lengthening of non-180° domain bands is energetically favourable compared to broadening because the lengthening process requires only the displacement of the ions near the tip of the domain while broadening involves displacement of ions along the length of the domain wall [115]. Nevertheless, broadening without lengthening can be expected when the lengthening mechanism is unavailable, for example due to pinning defects [115], or when blocked by other domain walls [62]. Figure 2.17 shows an example where a 180° domain wall effectively blocks the lengthening mechanism by enforcing an unfavourable polarization orientation relative to the applied electric field.

2.7.3 Checkerboard pattern 2: Simultaneous broadening and lengthening of needle-like domain structure

In figure 2.17, the broadening of lamellar structures without lengthening was observed, however, simultaneous lengthening and broadening can also occur. In figure 2.18(a), needle-like structures in a tetragonal region are intersected by 180° domain boundaries (marked by C_1). Comparing the widths of three of these needles, marked C_2 in figures 2.18(a) and (f), it is evident that there was significant broadening during the electrical loading process. The average needle width, measured at the section marked by a dotted line in figures 2.18(a) and (f) increased from 83 nm to 168 nm. In the series of PFM images from figures 2.18(a)–(f), however, the needles have also extended in length. The needles at C_3 extend substantially between figures 2.18(c) and (d), during the application of 0.9 MVm^{-1} electric field. Similarly, needles C_4 extend substantially from figures 2.18(d)–(e) and by figure 2.18(f) most of the needles have reached the grain boundary C_5. By contrast, broadening of needles was a more gradual process, taking place over the whole series of loading steps.

Figure 2.18(g) is a schematic of the area marked 'g' in figures 2.18(a) and (f), showing the simultaneous lengthening and broadening of the needle domains. The needle growth is favoured by electric field: for example, the [001] regions of needle with $\theta_{\mathbf{p},\mathbf{E}} = 29°$ grow into a surrounding [100] domain with $\theta_{\mathbf{p},\mathbf{E}} = 73°$, allowing simultaneous broadening and lengthening of non-180° domain bands at the expense of the neighbouring domain. It is interesting to note, however, that the $[00\bar{1}]$ bands grow relative to the adjacent $[\bar{1}00]$ material, despite the unfavourable direction of polarization with regard to applied electric field in this case. This appears to happen in order to maintain compatibility with the growing [001] regions.

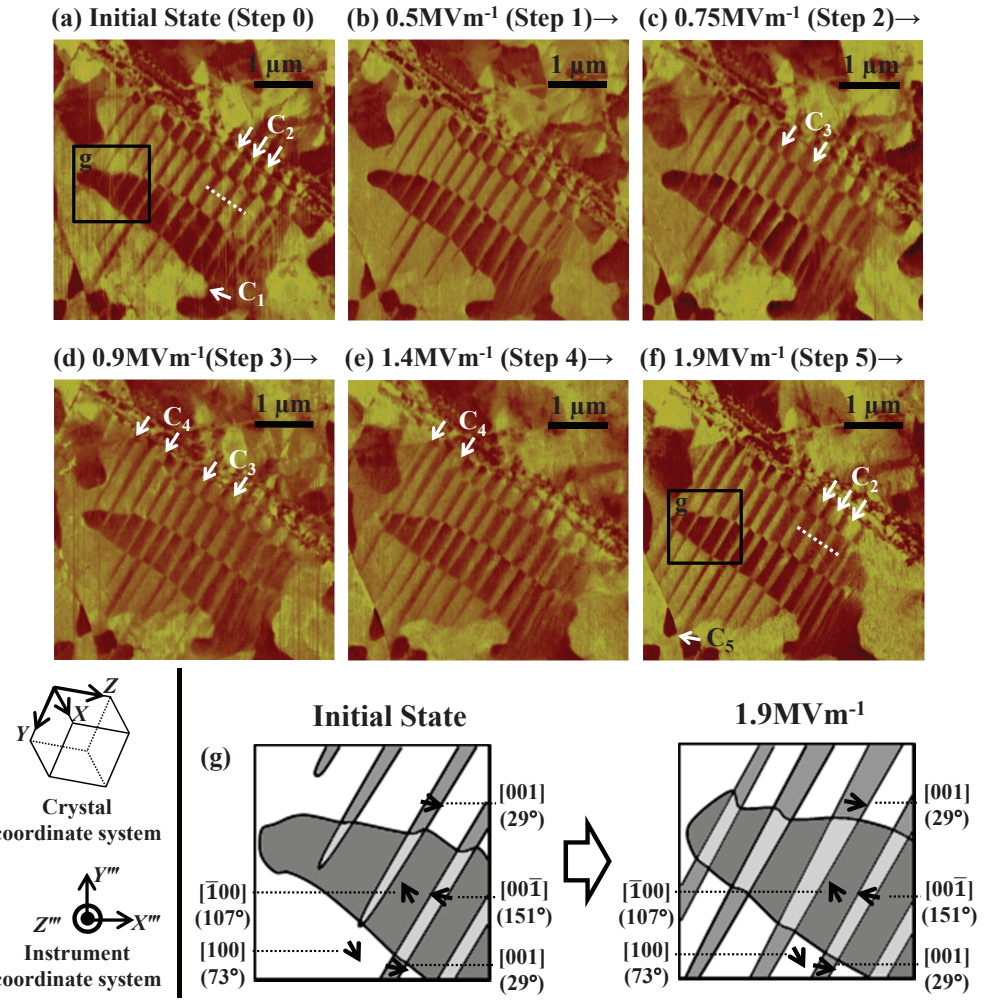

Figure 2.18: (a)–(f) PFM images of needle-like structures in a checkerboard pattern showing simultaneous broadening and lengthening. (g) Schematic of the pattern showing polarization directions.

The main changes in the PFM images occurred at electric field strengths of about $0.9-1.9\ \mathrm{MVm^{-1}}$. However, about 60% of the change in electric displacement occurred at fields of less than $0.9\ \mathrm{MVm^{-1}}$ according to figure 2.7(b). This is consistent across the majority of the PFM observations. This apparent contradiction can be resolved by noting that the PFM probes only the domain structure of the surface material, due to field lines diverging away from the probe. Thus, the output piezoresponse is dominated by a top layer of thickness a few times the probe tip radius (20 nm). The polarization evolution process at the surface of a bulk sample is expected to differ from that in the bulk because

of the electrical and mechanical boundary conditions at the free surface. Thus, the domain evolution processes observed at surfaces in the PFM images are not necessarily representative of the bulk of the material. Note also that the domain structure was measured in the unloaded state after each application of electric field. Consequently, any domain evolution process that reversed during unloading would not be observed. Gradual back-switching of domains after electrical unloading, due to depolarization field, has been observed in thin films by Roelofs *et al*. [116]. In the present work, this effect is expected to be less pronounced because poling was conducted using nominally uniform field applied by remote electrodes. Furthermore, the measurements are taken at the free surface of bulk samples and so constraint is less severe than in the case of a thin film. Nevertheless, prior studies have also noted changes in domain pattern during unloading of bulk material [61]. Similar back-switching may have occurred prior to these observations.

2.8 Conclusion

Non-180° domain evolution in bulk polycrystalline PZT during poling was studied using PFM *via* two different experimental methods. It is found that histograms of pixel intensity in PFM images are dome-shaped in unpoled regions of material and M-shaped in strongly poled regions. Correlating this observation with the PFM images themselves suggests that the presence of fine non-180° domain structures produces regions of intermediate contrast resulting in the dome shaped distributions. Coarser 180° watermark domains give the bi-modal M-shaped distributions. The evidence suggests the possibility that non-180° domain structure disappear from the sample surface during the poling process, specifically, during the saturation of the dielectric response, above the coercive field.

However, this provided only statistical evidence for the domain evolution of non-180° domain structure.

Therefore, for direct evidence of domain evolution, step-wise poling was conducted on PZT, interrupted by PFM scanning after each poling step. In a herringbone-like structure composed of two sets of lamellae angled to each other, one set of lamellae expands at the expense of the other, and in the end, the herringbone structure is transformed into a single lamination. In a checkerboard pattern of intersecting 90° and 180° domains, both the broadening of lamellae without lengthening, and the simultaneous broadening and lengthening of lamellae were observed. Broadening without lengthening occurred where lengthening would involve the growth of an unfavourable polarization direction with respect to the neighbouring domain. In general, domains grew according to the principle that the domain whose polarization direction was closest to the applied electric field vector was favoured. However, in some cases domains grew contrary to this rule. This appeared to happen in order to maintain compatibility with other domains evolving according to the rule. Finally, in complex domain patterns consisting of 180° and non-180° domain walls, 180° and non-180° polarization switching were observed to occur together.

The findings suggest that models for domain evolution should take account of the way domains interact, not just consider switching of individual domains. And, the methods developed provide a way to identify ferroelectric domains, but the method required a certain degree of insight and systematic interpretation. It would be desirable to find a way to extract more data from PFM signals. Finally, the testing involved only electric field. Thus, it would be valuable to consider also the effects of stress.